The Astrophysical Journal Supplement Series, 172:368–382, 2007 September

THE *XMM-NEWTON* WIDE-FIELD SURVEY IN THE COSMOS FIELD. IV. X-RAY SPECTRAL PROPERTIES OF ACTIVE GALACTIC NUCLEI[1]

V. Mainieri,[2,3] G. Hasinger,[2] N. Cappelluti,[2] M. Brusa,[2] H. Brunner,[2] F. Civano,[4] A. Comastri,[4] M. Elvis,[5] A. Finoguenov,[2] F. Fiore,[6] R. Gilli,[4] I. Lehmann,[2] J. Silverman,[2] L. Tasca,[7] C. Vignali,[4] G. Zamorani,[4] E. Schinnerer,[8] C. Impey,[9] J. Trump,[9] S. Lilly,[10] C. Maier,[10] R. E. Griffiths,[11] T. Miyaji,[11] P. Capak,[12] A. Koekemoer,[13] N. Scoville,[12,14] P. Shopbell,[12] and Y. Taniguchi[15]

Received 2006 April 24; accepted 2006 December 5

ABSTRACT

We present a detailed spectral analysis of pointlike X-ray sources in the *XMM-Newton* COSMOS field. Our sample of 135 sources only includes those that have more than 100 net counts in the 0.3–10 keV energy band and have been identified through optical spectroscopy. The majority of the sources are well described by a simple power-law model with either no absorption (76%) or a significant intrinsic, absorbing column (20%). The remaining ∼4% of the sources require a more complex modeling by incorporating additional components to the power law. For sources with more than 180 net counts (bright sample), we allowed both the photon spectral index Γ and the equivalent hydrogen column $N_{\rm H}$ to be free parameters. For fainter sources, we fix Γ to the average value and allow $N_{\rm H}$ to vary. The mean spectral index of the 82 sources in the bright sample is $\langle\Gamma\rangle = 2.06 \pm 0.08$, with an intrinsic dispersion of ∼0.24. Each of these sources has fractional errors on the value of Γ below 20%. As expected, the distribution of intrinsic absorbing column densities is markedly different between AGNs with or without broad optical emission lines. We find within our sample four type 2 QSO candidates ($L_{\rm X} > 10^{44}$ ergs s^{-1}, $N_{\rm H} > 10^{22}$ cm^{-2}), with a spectral energy distribution well reproduced by a composite Seyfert 2 spectrum, that demonstrates the strength of the wide-field COSMOS *XMM-Newton* survey to detect these rare and underrepresented sources. In addition, we have identified a Compton-thick ($N_{\rm H} > 1.5 \times 10^{24}$ cm^{-2}) AGN at $z = 0.1248$. Its X-ray spectrum is well fitted by a pure reflection model and a significant Fe Kα line at rest-frame energy of 6.4 keV.

Subject headings: galaxies: active — surveys — X-rays: diffuse background — X-rays: galaxies — X-rays: general

Online material: color figures

1. INTRODUCTION

Deep pencil-beam surveys with *ROSAT* (Hasinger et al. 1998), *Chandra* (Brandt et al. 2001; Rosati et al. 2002; Cowie et al. 2002; Alexander et al. 2003), and *XMM-Newton* (Hasinger et al. 2001; Loaring et al. 2005) have proved that the majority of the X-ray background (XRB) is generated by active galactic nuclei (AGNs) in both the soft (0.5–2 keV) and the hard (2–10 keV) bands. At fluxes below $\sim 10^{-14}$ ergs cm^{-2} s^{-1} in the hard band, the X-ray source population in these surveys is mainly composed of obscured AGNs. This supports the suggestion by Setti & Woltjer (1989) that the spectral shape of the XRB is due to the integrated contribution of AGNs affected by photoelectric obscuration with a wide range of gas column density ($N_{\rm H}$) and redshifts. Since the resolved fraction of the XRB drops from ≈80%–90% at 2–6 keV to 50%–70% at 6–10 keV (Worsley et al. 2005), a sizable number of strongly absorbed AGNs may still be missing in the X-ray surveys. An alternative method to detect heavily absorbed AGNs is to select objects that have mid-IR and radio emission typical of AGNs, but faint near-IR and optical fluxes (Martinez-Sansigre et al. 2005). While this kind of study cannot quantify which fraction of these mid-IR selected, absorbed AGNs would be detected by X-ray selection, the COSMOS survey (Scoville et al. 2007) will be able to answer this question due to its rich multiwavelength coverage (from radio to X-ray) on a large area of the sky (2 deg^2). The *XMM-Newton* wide-field survey in the COSMOS field (COSMOS *XMM-Newton*; Hasinger et al. 2007), with an unprecedented combination of wide area coverage and high sensitivity, is providing a large number of AGNs with enough counts to perform a detailed study of their X-ray spectra. This spectral information, particularly the $N_{\rm H}$ distribution, is a fundamental input parameter

[1] Based on observations obtained with *XMM-Newton*, an ESA science mission with instruments and contributions directly funded by ESA Member States and NASA.

[2] Max Planck Institut für Extraterrestrische Physik, Giessenbachstrasse 1, D-85748 Garching, Germany.

[3] European Southern Observatory, Karl-Schwarzschild-Strasse 2, D-85748 Garching, Germany.

[4] INAF-Osservatorio Astronomico di Bologna, via Ranzani 1, I-40127 Bologna, Italy.

[5] Harvard-Smithsonian Center for Astrophysics, 60 Garden Street, Cambridge, MA 02138.

[6] INAF-Osservatorio Astronomico di Roma, via Frascati 33, I-00040 Monteporzio Catone (Roma), Italy.

[7] Laboratoire d'Astrophysique de Marseille, UMR 6110 CNRS-Université de Provence, BP8, 13376 Marseille Cedex 12, France.

[8] Max Planck Institut für Astronomie, Königstuhl 17, Heidelberg D-69117, Germany.

[9] Steward Observatory, University of Arizona, 933 North Cherry Avenue, Tucson, AZ 85721.

[10] Department of Physics, ETH Zurich, CH-8093 Zurich, Switzerland.

[11] Department of Physics, Carnegie Mellon University, 5000 Forbes Avenue, Pittsburgh, PA 15213.

[12] California Institute of Technology, MC 105-24, 1200 East California Boulevard, Pasadena, CA 91125.

[13] Space Telescope Science Institute, 3700 San Martin Drive, Baltimore, MD 21218.

[14] Visiting Astronomer, University of Hawaii, 2680 Woodlawn Drive, Honolulu, HI 96822.

[15] Physics Department, Graduate School of Science & Engineering, Ehime University, Bunkyo-cho 2-5, Matsuyama, Ehime 790-8577, Japan.

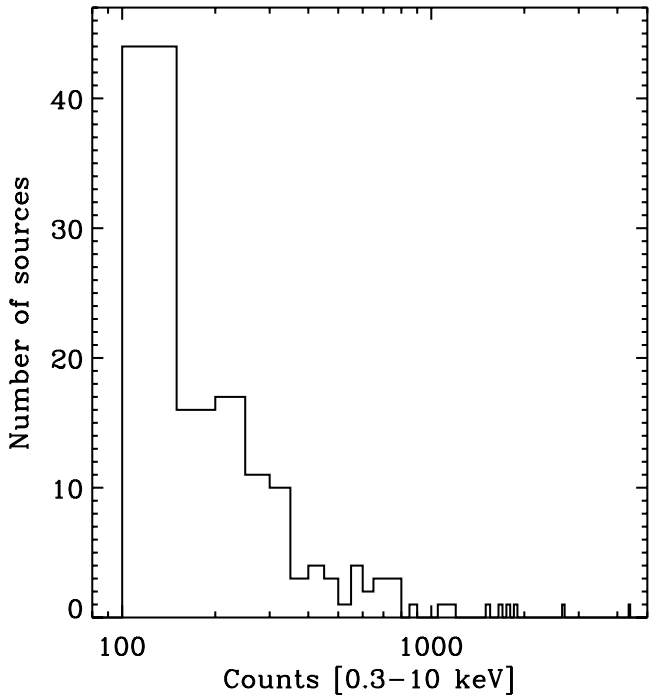

FIG. 1.—Net 0.3–10 keV pn counts distribution for the sample of 135 X-ray sources used in this work.

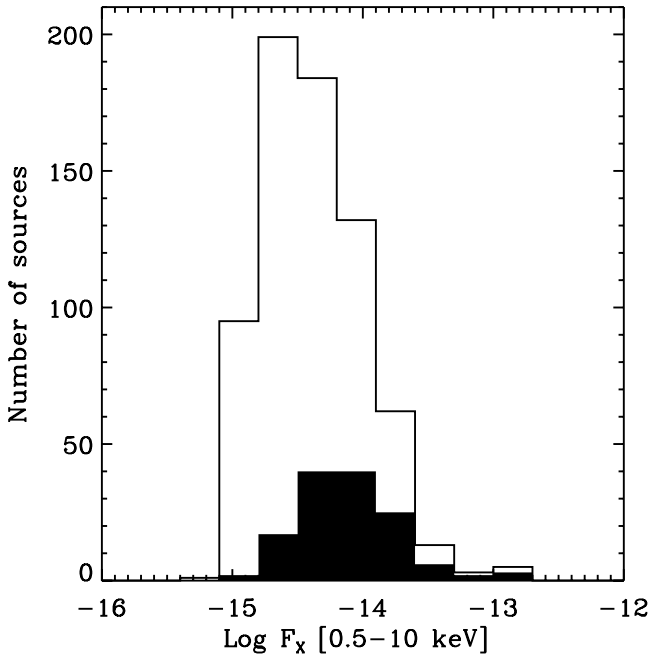

FIG. 2.—X-ray 0.5–10 keV flux distribution for all the X-ray sources (*open histogram*) and for the sample of spectroscopically identified sources (*filled histogram*), with more than 100 net counts, we analyze in this work. [*See the electronic edition of the Supplement for a color version of this figure.*]

to model the XRB (e.g., Comastri et al. 1995; Gilli et al. 2001). While we anticipate the completion of the multiwavelength campaigns including the optical spectroscopic follow-up within the next few years, we report in this paper the X-ray spectral fitting results for a preliminary sample of spectroscopically identified X-ray sources. The paper is structured as follows: in § 2 we describe the sample selected on the basis of counts statistics and optical identification; in § 3 we describe our X-ray spectral extraction procedure; in § 4 we present the results of the X-ray spectral analysis; in § 5 we discuss the properties of four type 2 QSOs; in § 6 we compare the X-ray and optical classification; and finally we summarize our conclusions in § 7. Throughout the paper we assume $H_0 = 70$ km s^{-1} Mpc^{-1}, $\Omega_m = 0.3$, and $\Omega_\Lambda = 0.7$.

2. SAMPLE SELECTION

XMM-Newton has imaged the full 2 deg^2 of the COSMOS area down to the following flux limits in the respective energy bands: 7×10^{-16} ergs cm^{-2} s^{-1} (0.5–2 keV), 4.0×10^{-15} ergs cm^{-2} s^{-1} (2–10 keV), and 1.0×10^{-14} ergs cm^{-2} s^{-1} (5–10 keV; see Fig. 7 of Cappelluti et al. [2007] for details on the sky coverage as a function of the X-ray flux). A general outline of the survey can be found in Hasinger et al. (2007). Further details such as the point-source detection method and sky area coverage as a function of the X-ray flux are presented in Cappelluti et al. (2007). Our sample is based on the X-ray catalog of 1390 pointlike sources (Cappelluti et al. 2007). We limit our analysis to the sources detected with the EPIC pn-CCD (pn) camera (Strüder et al. 2001), in the first 12 COSMOS *XMM-Newton* observations, since optical spectroscopic follow-up (Trump et al. 2007; Lilly et al. 2007) has been concentrated in this area ($\sim$1.3 deg^2). These 12 fields are flagged in Table 1 of Hasinger et al. (2007). Reliable optical counterparts (Brusa et al. 2007) have been determined for $\sim$90% of the sources in these 12 fields. We exclude 20 of the 715 X-ray sources in this area that are classified as "extended" from the detection algorithm. The observed X-ray emission from these sources is likely to be due to a group or cluster of galaxies, while here we are interested in selecting AGNs. From the remaining 695 X-ray sources, we select sources with greater than 100 net counts in the 0.3–10 keV energy band and optical spectroscopic identification. We further remove one source that has been identified as a star (Trump et al. 2007). The final sample comprises 135 objects. We show the distribution of their net counts in the 0.3–10 keV band in Figure 1 and the 0.5–10 keV flux distribution (Fig. 2) that covers a range of 1.4×10^{-15} to 1.2×10^{-13} ergs cm^{-2} s^{-1}. From their optical spectra, we can further subdivide our sample based on the presence of broad emission lines: broad-line AGNs (BL AGNs, 86 objects; FWHM > 2000 km s^{-1}), non-broad-line AGNs (NOT BL AGNs, 49 objects; FWHM < 2000 km s^{-1}). We note that in this latter class there are objects showing clear signs of nuclear activity such as high-excitation emission lines, as well as sources with normal galaxy spectra. We compare this purely optical classification with the X-ray properties of our sources in § 6.

3. EXTRACTION OF X-RAY SPECTRAL PRODUCTS

We have implemented an automated procedure to produce the X-ray spectrum for each source by combining counts from individual exposures. We have used the latest release of the *XMM-Newton* Science Analysis System (SAS)[16] software package (ver. 7.0). The task `region` has been used to generate the source and background extraction regions. The source region is defined as a circle with radius r_s that varies according to the signal-to-noise and the off-axis angle of the detection to optimize the quality of the final spectrum. The radii of these regions are reduced by the task to avoid overlapping with the extraction regions of nearby sources. All source regions are further excised from the area used for the background measurement. The task `especget` has been used to extract from the event file the source and background spectra for each object. The same task generates the calibration matrices (i.e., arf and rmf) for each spectrum and

[16] See http://xmm.vilspa.esa.es/external/xmm_sw_cal/sas_frame.shtml.

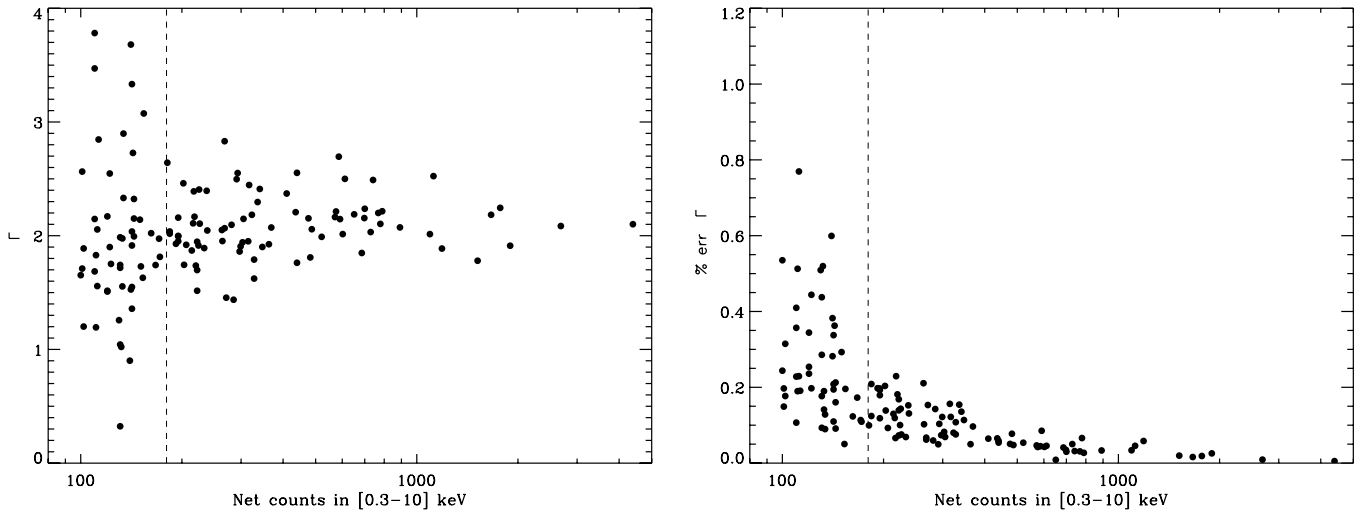

FIG. 3.—*Left*: Spectral slope value (Γ) from the fit of each single source using the PL model as a function of the net counts in the full 0.3–10 keV band. *Right*: Fractional statistical error (1 σ) on Γ as a function of the net counts in the 0.3–10 keV energy band. The dashed line in both plots is the threshold of 180 net counts in the 0.3–10 keV band that divides the bright from the faint sample. [*See the electronic edition of the Supplement for a color version of this figure*.]

determines the size of the source and background areas while updating the keyword BACKSCAL in the header of the spectra appropriately.[17] The single pointing spectra have been combined with `mathpha` to generate the spectrum of the whole observation.[18] For each source in our sample, we use all the available counts from the COSMOS *XMM-Newton* observations, including those coming from overlapping fields not included in the 12 fields list (see Fig. 1 of Hasinger et al. 2007). Finally, in order to use the χ^2 minimization technique, we bin the spectra with `grppha` so that each bin has at least 20 counts.

4. SPECTRAL ANALYSIS

Tozzi et al. (2006) have shown by extensive simulations that below 50 counts the best-fit values obtained using Cash statistics (Cash 1979) are more accurate than those obtained with the χ^2. For greater than 50 counts, the two methods give equivalent results. Since we limit our analysis in this paper to sources with more than 100 counts, we are confident that the results obtained with the χ^2 minimization technique are accurate. We use XSPEC[19] (ver. 11.3.2p) for our spectral fitting analysis. We first fit the data with two basic input models: a simple `powerlaw` (PL) and a `powerlaw` modified by intrinsic absorption at the redshift of the source (APL). Both models include an additional component to account for photoelectric absorption due to the Galactic column density that is fixed to the value in the COSMOS region ($N_{\rm H}^{\rm Gal} \sim 2.7 \times 10^{20}$ cm^{-2}; Dickey & Lockman 1990).[20] The PL model is made of two XSPEC components `wabs*zpowerlw`, while the APL model consists of the combination of three different components `wabs*zwabs*zpowerlw`. The `wabs` model describes the photoelectric absorption using Wisconsin cross-sections (Morrison & McCammon 1983) and its only parameter is the equivalent hydrogen column density (`zwabs` has the redshift as an additional parameter). The `zpowerlw` model is a simple power law parameterized by the photon index, the redshift, and a normalization factor.[21] The model fits yield the power-law photon index Γ, the X-ray luminosity in the 0.5–2 and 2–10 keV rest-frame bands, and from the APL model also the intrinsic column density $N_{\rm H}$. We notice that the dispersion of Γ for our sample increases significantly for sources with low count statistics (Fig. 3, *left*), and in particular the fractional error becomes quite large (Fig. 3, *right*). Above 180 net counts, the fractional error remains below 20%. Hence, we split our sample in two: sample 1 including 82 sources with more than 180 net counts, and sample 2 having 53 sources with fewer than 180 counts. For sample 1, we allow both Γ and $N_{\rm H}$ free to vary, while we fix Γ to the average value, obtained with sample 1, for lower count sources (sample 2). For all the 135 X-ray sources, we perform a spectral fit using both PL and APL models. We label a source as X-ray absorbed in those cases for which the APL model is a better fit, than the pure PL, with a confidence level threshold of 90% based on an *F*-test. The output of our spectral analysis is reported in Table 1. The table has the following structure: IAU name (col. [1]), identification number (xid, col. [2]), X-ray coordinates (cols. [3]–[4]), net detected X-ray counts in the 0.3–10 keV band (col. [5]), spectroscopic redshift (col. [6]), best-fit model (col. [7]), spectral index Γ (col. [8]), intrinsic column density $N_{\rm H}$ (col. [9]), X-ray fluxes (cols. [10]–[12]), de-absorbed X-ray luminosities (cols. [13]–[15]).

4.1. *Notes on Some Individual Sources*

For each source we carefully check the results obtained with the basic PL and APL models and, if significant residuals are present, we refine the fit using more complex models. We show in Figure 4 a representative X-ray spectrum for each one of the different best-fit models. We use the *F*-test and a confidence level threshold of 90% to choose between the different models.

4.1.1. *Soft Excess*

A clear *soft excess* is present in four of our sources (xid 41, 106, 117, 274). This feature, first observed with *EXOSAT* (Arnaud et al. 1985; Turner & Pounds 1989), has been confirmed by *XMM-Newton* observations (e.g., Pounds & Reeves 2002; Porquet et al.

[17] The header keyword BACKSCAL is set to 1 for the source spectrum, while for the background spectrum it is fixed to the ratio of the background to the source areas.

[18] We note that all the *XMM-Newton* observations in the COSMOS field have been performed with the thin filter for the pn camera.

[19] See http://heasarc.gsfc.nasa.gov/docs/xanadu/xspec.

[20] This is an average value for the Galactic $N_{\rm H}$ in the COSMOS area, where $N_{\rm H}^{\rm Gal}$ is in the range $(2.5–2.9) \times 10^{20}$ cm^{-2}. This range in Galactic column density does not affect the results of our spectral analysis.

[21] We refer the reader to http://heasarc.gsfc.nasa.gov/xanadu/xspec/manual/Models.html for further details on the spectral models.

TABLE 1

X-Ray Spectral Fit Parameters

IAU[a]	XID[b]	R.A.[c] (J2000.0)	Decl.[c] (J2000.0)	Counts[d] 0.3–10	z[e]	Model[f]	Γ	$N_{\rm H}$	$f_{\rm X}$[g] 0.5–2	$f_{\rm X}$[g] 2–10	$f_{\rm X}$[g] 0.5–10	$L_{\rm X}$[h] 0.5–2	$L_{\rm X}$[h] 2–10	$L_{\rm X}$[h] 0.5–10
XMMC J100025.30+015851.2	1	10 00 25.30	1 58 51.19	4396	0.373	PL	$2.11^{+2.15}_{-2.08}$	...	746.88	795.94	1542.80	43.55	43.58	43.87
XMMC J095857.50+021314.1	2	9 58 57.50	2 13 14.10	1896	1.024	PL	$1.79^{+1.84}_{-1.75}$	...	1178.70	2004.80	3183.60	44.81	45.05	45.25
XMMC J095902.83+021906.8	3	9 59 02.83	2 19 06.77	2683	0.345	PL	$2.07^{+2.12}_{-2.03}$	...	1318.50	1484.60	2803.10	43.72	43.77	44.05
XMMC J095858.68+021458.1	4	9 58 58.68	2 14 58.12	1188	0.132	PL	$1.78^{+1.84}_{-1.71}$	...	851.43	1491.50	2342.90	42.59	42.84	43.03
XMMC J095918.91+020951.3	5	9 59 18.91	2 09 51.26	1517	1.154	PL	$1.78^{+1.84}_{-1.72}$	...	377.01	659.48	1036.50	44.45	44.69	44.89
XMMC J100043.26+020636.6	6	10 00 43.26	2 06 36.56	1664	0.360	PL	$2.18^{+2.26}_{-2.11}$	...	388.08	377.01	765.09	43.25	43.23	43.54
XMMC J100013.02+023521.8	8	10 00 13.02	2 35 21.82	1121	0.699	PL	$2.45^{+2.53}_{-2.38}$	...	627.74	407.25	1035.00	44.13	43.95	44.35
XMMC J095940.86+021938.6	9	9 59 40.86	2 19 38.56	1094	1.459	PL	$1.99^{+2.08}_{-1.91}$	...	196.07	249.26	445.33	44.42	44.52	44.77
XMMC J100034.95+020234.0	11	10 00 34.95	2 02 34.03	789	1.177	PL	$2.25^{+2.37}_{-2.13}$	...	139.90	122.46	262.35	44.04	43.98	44.31
XMMC J100049.95+020500.0	12	10 00 49.95	2 05 00.03	741	1.235	PL	$2.50^{+2.63}_{-2.38}$	...	240.22	144.84	385.06	44.33	44.11	44.53
XMMC J095924.69+015954.5	17	9 59 24.69	1 59 54.45	1771	1.236	PL	$2.23^{+2.30}_{-2.16}$	...	728.21	653.76	1382.00	44.81	44.76	45.09
XMMC J095958.60+021531.0	19	9 59 58.60	2 15 31.02	487	0.658	PL	$2.05^{+2.20}_{-1.90}$	...	247.59	278.06	525.65	43.63	43.70	43.97
XMMC J100058.80+022556.7	20	10 00 58.80	2 25 56.68	575	0.693	PL	$2.22^{+2.34}_{-2.10}$	...	182.66	165.75	348.41	43.62	43.58	43.90
XMMC J100055.46+023442.0	21	10 00 55.46	2 34 41.99	571	1.403	PL	$2.15^{+2.28}_{-2.02}$	...	158.63	159.81	318.44	44.28	44.29	44.58
XMMC J100046.85+020405.2	22	10 00 46.85	2 04 05.25	586	0.552	PL	$2.70^{+2.84}_{-2.56}$	...	113.30	51.61	164.91	43.11	42.77	43.27
XMMC J095909.63+021917.2	23	9 59 09.63	2 19 17.22	891	0.378	PL	$2.05^{+2.16}_{-1.95}$	...	314.47	360.31	674.78	43.17	43.23	43.50
XMMC J100024.74+023148.3	24	10 00 24.74	2 31 48.34	382	1.318	PL	$2.65^{+2.79}_{-2.51}$	...	293.47	143.55	437.02	44.48	44.17	44.66
XMMC J100024.55+020618.5	25	10 00 24.55	2 06 18.48	440	2.281	PL	$1.75^{+1.88}_{-1.62}$	...	156.54	286.15	442.68	44.79	45.06	45.25
XMMC J095949.51+020139.1	30	9 59 49.51	2 01 39.09	611	1.758	PL	$2.51^{+2.67}_{-2.35}$	...	120.90	72.33	193.24	44.41	44.18	44.61
XMMC J095947.05+022209.4	31	9 59 47.05	2 22 09.38	700	0.909	PL	$2.27^{+2.40}_{-2.15}$	...	128.42	108.14	236.56	43.72	43.65	43.99
XMMC J100114.36+022357.5	33	10 01 14.36	2 23 57.47	410	1.799	PL	$2.34^{+2.50}_{-2.19}$	...	119.16	91.12	210.28	44.42	44.31	44.67
XMMC J095958.62+021805.9	34	9 59 58.62	2 18 05.92	521	1.792	PL	$1.99^{+2.14}_{-1.85}$	...	111.88	142.74	254.62	44.39	44.50	44.75
XMMC J095928.45+022107.6	35	9 59 28.45	2 21 07.64	440	0.346	PL	$2.54^{+2.68}_{-2.40}$	...	117.30	67.04	184.34	42.72	42.47	42.91
XMMC J095940.18+022306.3	37	9 59 40.18	2 23 06.28	698	1.132	PL	$2.16^{+2.29}_{-2.06}$	...	89.97	89.38	179.35	43.81	43.80	44.10
XMMC J100058.94+015359.5	38	10 00 58.94	1 53 59.45	369	1.559	APL	$2.04^{+2.19}_{-1.85}$	$20.73^{+21.46}_{-20.42}$	106.94	129.53	236.47	44.32	44.39	44.65
XMMC J100114.94+020208.9	40	10 01 14.94	2 02 08.93	602	0.989	PL	$2.01^{+2.14}_{-1.89}$	...	465.40	574.11	1039.50	44.37	44.47	44.72
XMMC J100025.43+020734.4	41	10 00 25.43	2 07 34.43	315	0.114	APL+po	$1.95^{+2.37}_{-1.65}$	$21.51^{+21.55}_{-21.27}$	76.89	204.98	281.87	41.63	41.76	42.00
XMMC J100202.80+022435.8	42	10 02 02.80	2 24 35.82	476	0.988	PL	$2.15^{+2.32}_{-1.99}$	...	197.35	197.84	395.20	44.00	44.00	44.30
XMMC J100051.57+021215.8	44	10 00 51.57	2 12 15.80	305	1.829	PL	$2.14^{+2.32}_{-1.99}$	...	105.65	107.47	213.13	44.39	44.40	44.69
XMMC J100014.12+020054.2	51	10 00 14.12	2 00 54.18	336	2.497	PL	$1.98^{+2.26}_{-1.88}$	...	50.78	65.43	116.21	44.44	44.55	44.80
XMMC J100016.35+015104.3	52	10 00 16.35	1 51 04.30	297	1.135	PL	$1.85^{+2.00}_{-1.70}$	...	107.96	169.84	277.80	43.82	44.02	44.23
XMMC J100131.15+022924.8	54[i]	10 01 31.15	2 29 24.82	246	0.350	R-S	...	...	90.18	24.44	114.62	42.57	42.00	42.67
XMMC J100001.16+021413.9	56	10 00 01.16	2 14 13.92	110	1.407	PL	2.00	...	89.25	101.56	190.81	44.04	44.09	44.37
XMMC J100047.09+020017.7	59	10 00 47.09	2 00 17.71	226	1.904	PL	$2.12^{+2.33}_{-1.93}$	...	59.74	63.30	123.04	44.18	44.21	44.50
XMMC J095907.84+020819.3	63	9 59 07.84	2 08 19.34	264	0.354	PL	$1.95^{+2.19}_{-1.73}$	...	193.50	260.69	454.19	42.85	42.98	43.22
XMMC J095934.63+020627.9	64	9 59 34.63	2 06 27.94	299	0.686	PL	$1.64^{+1.81}_{-1.47}$	...	56.23	121.35	177.58	43.00	43.34	43.50
XMMC J100041.87+022411.1	65	10 00 41.87	2 24 11.07	122	0.979	PL	2.00	...	61.79	77.64	139.44	43.49	43.59	43.84
XMMC J095928.45+021950.5	66	9 59 28.45	2 19 50.47	436	1.488	PL	$2.22^{+2.40}_{-2.04}$	...	81.58	74.39	155.96	44.06	44.02	44.34
XMMC J100137.74+022845.1	67	10 01 37.74	2 28 45.09	224	0.367	PL	$1.93^{+2.16}_{-1.71}$	...	69.35	97.21	166.56	42.37	42.51	42.75
XMMC J095934.92+021028.5	69	9 59 34.92	2 10 28.46	133	2.412	PL	2.00	...	78.25	98.32	176.57	44.55	44.65	44.91
XMMC J100036.13+022830.7	70	10 00 36.13	2 28 30.66	181	0.688	APL	$2.78^{+3.92}_{-2.27}$	$23.23^{+23.41}_{-23.04}$	25.19	579.88	605.07	44.68	44.29	44.83
XMMC J100129.81+023239.6	72	10 01 29.81	2 32 39.56	220	0.825	APL	$1.72^{+2.04}_{-1.40}$	$21.00^{+21.47}_{-20.42}$	55.72	114.19	169.91	43.33	43.61	43.80
XMMC J100031.66+014757.4	75	10 00 31.66	1 47 57.40	363	1.681	PL	$1.94^{+2.10}_{-1.80}$	...	154.44	211.03	365.48	44.46	44.60	44.84
XMMC J100028.71+021744.5	78	10 00 28.71	2 17 44.48	203	1.039	PL	$1.72^{+2.02}_{-1.45}$	...	50.69	95.86	146.54	43.46	43.74	43.93
XMMC J100124.93+022032.2	79	10 01 24.93	2 20 32.19	171	1.708	PL	2.00	...	74.53	93.65	168.18	44.16	44.26	44.52
XMMC J100105.65+015603.0	81	10 01 05.65	1 56 03.04	285	0.915	APL	$1.44^{+1.65}_{-1.23}$	$21.44^{+21.67}_{-20.94}$	50.50	159.64	210.14	43.26	43.70	43.84
XMMC J100117.73+023309.0	85	10 01 17.73	2 33 09.02	184	1.001	APL	$1.99^{+2.42}_{-1.58}$	$21.16^{+21.63}_{-20.42}$	50.33	68.88	119.21	43.50	43.60	43.85

TABLE 1—*Continued*

IAU[a]	XID[b]	R.A.[c] (J2000.0)	Decl.[c] (J2000.0)	Counts[d] 0.3–10	z[e]	Model[f]	Γ	$N_{\rm H}$	$f_{\rm X}$[g] 0.5–2	$f_{\rm X}$[g] 2–10	$f_{\rm X}$[g] 0.5–10	$L_{\rm X}$[h] 0.5–2	$L_{\rm X}$[h] 2–10	$L_{\rm X}$[h] 0.5–10
XMMC J100048.01+021128.0	94	10 00 48.01	2 11 28.00	142	1.515	PL	2.00	...	80.93	101.69	182.61	44.07	44.17	44.43
XMMC J100136.47+025304.5	96	10 01 36.47	2 53 04.50	134	2.117	PL	2.00	...	163.26	201.31	364.57	44.73	44.83	45.08
XMMC J100031.41+022819.2	101	10 00 31.41	2 28 19.18	131	0.926	PL	2.00	...	47.26	59.38	106.63	43.31	43.41	43.66
XMMC J100028.20+015547.0	103	10 00 28.20	1 55 46.98	144	1.519	PL	2.00	...	53.96	67.80	121.76	43.90	44.00	44.25
XMMC J100038.13+022455.8	106	10 00 38.13	2 24 55.79	141	0.710	APL+po	2.00	$22.33^{+22.66}_{-21.98}$	14.54	43.92	58.47	42.85	42.95	43.20
XMMC J095935.73+020537.2	113	9 59 35.73	2 05 37.24	101	1.910	PL	2.00	...	55.61	69.87	125.48	44.16	44.26	44.51
XMMC J100210.73+023028.0	115	10 02 10.73	2 30 27.97	591	1.161	APL	$2.10^{+2.23}_{-1.95}$	$21.10^{+21.42}_{-20.42}$	176.22	204.96	381.18	44.18	44.22	44.50
XMMC J100049.61+021709.2	116	10 00 49.61	2 17 09.17	218	0.874	APL	$2.11^{+2.38}_{-1.61}$	$21.11^{+21.58}_{-20.42}$	74.38	87.32	161.71	43.53	43.56	43.84
XMMC J100013.45+021400.5	117	10 00 13.45	2 14 00.47	111	0.936	APL+po	2.00	$22.76^{+23.14}_{-22.37}$	28.01	35.20	63.21	43.09	43.19	43.45
XMMC J100122.23+021334.0	119	10 01 22.23	2 13 33.99	328	0.891	APL	$1.69^{+2.04}_{-1.40}$	$21.01^{+21.48}_{-20.42}$	213.98	452.80	666.78	43.97	44.27	44.44
XMMC J095945.47+021029.9	122	9 59 45.47	2 10 29.88	130	2.418	APL	2.00	$23.69^{+23.91}_{-23.44}$	14.90	147.41	162.32	44.83	44.93	45.18
XMMC J100131.93+023335.5	123	10 01 31.93	2 33 35.46	142	2.065	PL	2.00	...	23.93	30.07	54.00	43.87	43.97	44.23
XMMC J100001.27+022320.7	127	10 00 01.27	2 23 20.69	217	1.846	PL	$2.55^{+2.91}_{-2.22}$	...	34.62	19.63	54.25	43.91	43.67	44.11
XMMC J100047.85+020756.1	128	10 00 47.85	2 07 56.15	120	2.161	PL	2.00	...	32.52	40.86	73.38	44.06	44.15	44.41
XMMC J100100.90+015946.7	129	10 01 00.90	1 59 46.69	184	1.170	PL	$1.98^{+2.21}_{-1.76}$	...	196.94	256.78	453.72	44.13	44.25	44.49
XMMC J100105.36+021348.0	133	10 01 05.36	2 13 47.96	144	2.627	PL	2.00	...	56.73	71.28	128.00	44.50	44.60	44.86
XMMC J100011.78+021919.9	134	10 00 11.78	2 19 19.86	141	0.625	PL	2.00	...	35.13	44.14	79.28	42.76	42.86	43.12
XMMC J095949.98+020010.6	137	9 59 49.98	2 00 10.57	195	1.808	PL	$1.87^{+2.31}_{-1.48}$	...	44.24	92.96	137.20	44.06	44.25	44.47
XMMC J100033.55+015236.3	141	10 00 33.55	1 52 36.34	102	0.831	APL	2.00	$21.64^{+21.96}_{-21.19}$	51.21	85.40	136.61	43.36	43.45	43.71
XMMC J100013.46+022656.7	143	10 00 13.46	2 26 56.66	140	0.732	APL	2.00	$22.68^{+23.06}_{-22.38}$	29.41	194.21	223.62	43.62	43.72	43.97
XMMC J095938.49+020447.5	146	9 59 38.49	2 04 47.51	167	2.804	APL	2.00	$21.95^{+22.26}_{-21.23}$	53.36	73.96	127.32	44.59	44.69	44.94
XMMC J100053.93+021614.2	147	10 00 53.93	2 16 14.22	112	2.944	PL	2.00	...	26.82	33.70	60.52	44.30	44.40	44.65
XMMC J100052.57+021643.8	148	10 00 52.57	2 16 43.80	111	0.843	PL	2.00	...	41.34	51.94	93.27	43.15	43.25	43.50
XMMC J100124.00+021446.4	152	10 01 24.00	2 14 46.45	172	0.894	PL	2.00	...	88.13	110.74	198.87	43.54	43.64	43.90
XMMC J100108.44+022342.6	153	10 01 08.44	2 23 42.58	142	1.928	APL	2.00	$21.91^{+22.20}_{-21.40}$	33.00	49.24	82.24	44.02	44.12	44.37
XMMC J100108.59+020053.2	161	10 01 08.59	2 00 53.24	254	2.681	PL	$1.69^{+1.93}_{-1.46}$	...	75.27	149.97	225.25	44.65	44.95	45.12
XMMC J100118.55+015543.6	164	10 01 18.55	1 55 43.59	291	0.528	PL	$2.54^{+2.73}_{-2.36}$	...	176.15	100.11	276.25	43.32	43.07	43.51
XMMC J100043.30+021352.7	165	10 00 43.30	2 13 52.65	120	2.146	PL	2.00	...	25.58	32.14	57.73	43.94	44.04	44.30
XMMC J095917.44+021514.9	170	9 59 17.44	2 15 14.91	142	0.935	PL	2.00	...	37.05	46.55	83.59	43.21	43.31	43.57
XMMC J100128.19+021819.9	171	10 01 28.19	2 18 19.86	133	1.187	PL	2.00	...	34.80	43.72	78.52	43.44	43.54	43.80
XMMC J095921.15+020030.8	196	9 59 21.15	2 00 30.83	154	1.486	PL	2.00	...	56.39	70.85	127.24	43.89	43.99	44.25
XMMC J100047.93+014935.9	198	10 00 47.93	1 49 35.93	134	0.893	PL	2.00	...	46.55	58.49	105.04	43.26	43.36	43.62
XMMC J095858.95+020138.7	199	9 58 58.95	2 01 38.72	268	2.454	PL	$2.11^{+2.36}_{-1.92}$	...	161.11	171.30	332.41	44.88	44.91	45.20
XMMC J100105.90+015918.6	206	10 01 05.90	1 59 18.58	131	0.721	APL	2.00	$21.69^{+22.19}_{-20.99}$	29.60	53.14	82.74	43.00	43.10	43.35
XMMC J100058.47+015206.4	216	10 00 58.47	1 52 06.40	216	2.029	PL	$2.22^{+2.69}_{-1.84}$	...	42.84	39.07	81.91	44.11	44.07	44.39
XMMC J095956.08+014728.0	222	9 59 56.08	1 47 27.97	237	0.337	PL	$2.28^{+2.57}_{-2.01}$	...	73.53	61.26	134.79	42.57	42.49	42.83
XMMC J100139.88+023132.8	236	10 01 39.88	2 31 32.77	110	1.444	PL	2.00	...	12.81	16.09	28.90	43.22	43.32	43.57
XMMC J100046.86+014737.1	256	10 00 46.86	1 47 37.14	113	1.867	APL	2.00	$20.71^{+21.83}_{-20.42}$	55.75	70.92	126.67	44.22	44.32	44.57
XMMC J100042.36+014535.7	265	10 00 42.36	1 45 35.66	101	1.161	PL	2.00	...	38.62	48.52	87.14	43.47	43.56	43.82
XMMC J095910.00+022018.4	268	9 59 10.00	2 20 18.42	143	0.432	APL	2.00	$21.32^{+21.60}_{-20.89}$	34.78	56.34	91.12	42.49	42.59	42.84
XMMC J100005.52+023057.4	274	10 00 05.52	2 30 57.40	112	0.677	APL+po	2.00	$22.67^{+23.00}_{-22.18}$	18.30	104.83	123.13	43.26	43.36	43.62
XMMC J095929.40+022035.6	282	9 59 29.40	2 20 35.60	150	1.733	PL	2.00	...	18.24	22.92	41.16	43.57	43.67	43.92
XMMC J095902.45+022510.6	288	9 59 02.45	2 25 10.61	202	1.105	PL	$2.17^{+2.46}_{-1.91}$	...	35.06	34.23	69.29	43.30	43.29	43.60
XMMC J095927.04+015340.8	293	9 59 27.04	1 53 40.84	222	0.444	APL	$1.51^{+2.10}_{-1.21}$	$21.91^{+22.13}_{-21.70}$	136.15	666.98	803.13	43.28	43.69	43.83
XMMC J100016.65+021352.1	298	10 00 16.65	2 13 52.11	100	1.867	PL	2.00	...	23.63	29.70	53.33	43.76	43.86	44.11
XMMC J100049.94+015230.8	359	10 00 49.94	1 52 30.79	222	1.156	PL	$1.54^{+1.85}_{-1.28}$	...	35.99	89.17	125.16	43.35	43.74	43.89
XMMC J100118.89+020729.0	391	10 01 18.89	2 07 28.98	110	1.774	PL	2.00	...	50.15	62.98	113.13	44.03	44.13	44.39
XMMC J100006.35+023342.0	398	10 00 06.35	2 33 42.01	131	0.745	APL	2.00	$21.64^{+21.98}_{-21.19}$	40.43	69.95	110.38	43.15	43.25	43.51

TABLE 1—*Continued*

IAU[a]	XID[b]	R.A.[c] (J2000.0)	Decl.[c] (J2000.0)	Counts[d] 0.3–10	z[e]	Model[f]	Γ	$N_{\rm H}$	$f_{\rm X}$[g] 0.5–2	$f_{\rm X}$[g] 2–10	$f_{\rm X}$[g] 0.5–10	$L_{\rm X}$[h] 0.5–2	$L_{\rm X}$[h] 2–10	$L_{\rm X}$[h] 0.5–10
XMMC J095944.64+022626.2	416	9 59 44.64	2 26 26.22	102	0.992	APL	2.00	$22.19^{+22.57}_{-21.72}$	18.76	45.28	64.04	43.28	43.38	43.63
XMMC J100223.07+014715.1	2013	10 02 23.07	1 47 15.07	686	1.243	PL	$1.82^{+1.92}_{-1.73}$	...	428.34	700.54	1128.90	44.58	44.80	45.00
XMMC J095819.89+022903.8	2016	9 58 19.89	2 29 03.78	768	0.345	PL	$2.19^{+2.31}_{-2.07}$	...	385.27	373.31	758.58	43.21	43.19	43.50
XMMC J100234.40+015011.5	2020	10 02 34.40	1 50 11.51	651	1.506	PL	$2.25^{+2.37}_{-2.14}$	...	226.06	196.73	422.80	44.51	44.45	44.78
XMMC J100129.41+013633.7	2021	10 01 29.41	1 36 33.75	271	0.104	APL	$1.23^{+1.39}_{-1.01}$	$22.38^{+22.51}_{-22.24}$	163.24	4230.20	4393.50	42.39	43.12	43.19
XMMC J100211.31+013707.2	2028	10 02 11.31	1 37 07.15	293	0.784	APL+Fe	$2.55^{+2.79}_{-2.29}$	$21.83^{+21.95}_{-21.69}$	113.12	204.74	317.86	43.75	43.50	43.94
XMMC J100257.55+015405.6	2036	10 02 57.55	1 54 05.58	233	0.971	PL	$1.89^{+2.07}_{-1.71}$	...	284.95	423.49	708.44	44.14	44.31	44.54
XMMC J100033.51+013812.6	2040	10 00 33.51	1 38 12.61	317	0.520	PL	$2.28^{+2.47}_{-2.10}$	...	263.04	212.05	475.09	43.40	43.32	43.67
XMMC J100237.09+014648.3	2043	10 02 37.09	1 46 48.33	347	0.668	APL+Fe	$1.56^{+1.92}_{-1.31}$	$21.77^{+21.96}_{-21.52}$	172.69	608.59	781.28	43.55	43.93	44.08
XMMC J100303.04+015209.2	2046	10 03 03.04	1 52 09.19	341	1.800	PL	$2.23^{+2.43}_{-2.04}$	...	132.62	119.47	252.09	44.47	44.43	44.75
XMMC J100151.19+020032.8	2058	10 01 51.19	2 00 32.81	779	0.964	PL	$2.02^{+2.13}_{-1.91}$	...	285.44	348.97	634.41	44.13	44.22	44.48
XMMC J100229.27+014528.2	2071	10 02 29.27	1 45 28.21	328	0.876	PL	$1.58^{+1.73}_{-1.44}$	...	177.16	414.17	591.34	43.72	44.09	44.24
XMMC J100141.42+021031.8	2078	10 01 41.42	2 10 31.78	195	0.982	APL	$1.93^{+2.20}_{-1.59}$	$20.96^{+21.50}_{-20.42}$	135.04	197.89	332.93	43.85	44.00	44.23
XMMC J100238.78+013938.2	2080	10 02 38.78	1 39 38.25	238	1.315	PL	$1.87^{+2.02}_{-1.73}$	...	127.19	193.62	320.82	44.07	44.26	44.48
XMMC J100238.27+013747.8	2093	10 02 38.27	1 37 47.75	222	2.506	PL	$1.97^{+2.16}_{-1.79}$	...	131.93	172.73	304.66	44.82	44.94	45.18
XMMC J100214.21+020620.0	2096	10 02 14.21	2 06 20.02	482	1.265	PL	$1.64^{+1.75}_{-1.54}$	...	131.85	282.01	413.85	44.03	44.36	44.53
XMMC J100219.58+015536.9	2105	10 02 19.58	1 55 36.94	323	1.509	PL	$2.19^{+2.43}_{-1.97}$	...	74.17	70.26	144.43	44.03	44.01	44.32
XMMC J100305.20+015157.0	2118	10 03 05.20	1 51 57.04	195	0.969	APL	$2.14^{+2.61}_{-1.75}$	$20.99^{+21.58}_{-20.42}$	165.82	180.69	346.51	43.93	43.94	44.24
XMMC J095848.84+023442.3	2138	9 58 48.84	2 34 42.34	729	1.551	PL	$2.01^{+2.11}_{-1.90}$	...	121.90	151.84	273.74	44.28	44.37	44.63
XMMC J100230.13+014810.0	2152	10 02 30.13	1 48 10.01	281	0.626	PL	$2.21^{+2.57}_{-1.90}$	...	94.64	86.97	181.61	43.19	43.16	43.48
XMMC J100232.55+014009.5	2169	10 02 32.55	1 40 09.53	144	1.776	PL	2.00	...	72.41	90.98	163.39	44.19	44.29	44.55
XMMC J100141.11+021259.9	2191	10 01 41.11	2 12 59.88	225	0.621	PL	$2.27^{+2.53}_{-2.03}$	...	87.36	74.02	161.38	43.01	42.94	43.28
XMMC J100236.79+015948.5	2202	10 02 36.79	1 59 48.50	142	1.516	PL	2.00	...	65.21	79.78	144.99	43.98	44.07	44.33
XMMC J100038.40+013708.4	2211	10 00 38.40	1 37 08.37	153	1.251	PL	2.00	...	65.00	81.68	146.68	43.77	43.87	44.13
XMMC J100156.40+014811.0	2213	10 01 56.40	1 48 11.00	263	0.957	APL	$2.02^{+2.53}_{-1.64}$	$20.87^{+21.55}_{-20.42}$	71.18	91.34	162.52	43.54	43.63	43.89
XMMC J100226.77+014052.1	2218	10 02 26.77	1 40 52.05	123	0.247	PL	2.00	...	55.24	69.41	124.65	42.01	42.11	42.36
XMMC J100041.57+013658.7	2220	10 00 41.57	1 36 58.69	162	0.995	PL	2.00	...	73.60	92.48	166.08	43.58	43.68	43.93
XMMC J100156.31+020942.9	2232	10 01 56.31	2 09 42.91	131	1.641	PL	2.00	...	43.15	54.21	97.36	43.88	43.98	44.24
XMMC J100253.16+013457.8	2235	10 02 53.16	1 34 57.85	100	2.248	PL	2.00	...	65.71	81.11	146.82	44.40	44.49	44.75
XMMC J095904.34+022552.8	2237	9 59 04.34	2 25 52.75	192	0.941	APL	$1.78^{+2.41}_{-1.40}$	$22.74^{+22.96}_{-22.55}$	38.88	285.86	324.74	43.91	44.15	44.34
XMMC J100223.02+020639.5	2246	10 02 23.02	2 06 39.48	303	0.899	PL	$1.95^{+2.15}_{-1.76}$	...	69.93	94.68	164.61	43.41	43.54	43.78
XMMC J100243.88+020501.6	2261	10 02 43.88	2 05 01.59	206	1.234	PL	$1.97^{+2.27}_{-1.70}$	...	72.98	95.93	168.91	43.81	43.93	44.17
XMMC J100208.53+014553.7	2276	10 02 08.53	1 45 53.65	111	2.215	PL	2.00	...	31.49	39.56	71.05	44.07	44.17	44.42
XMMC J100158.05+014621.7	2289	10 01 58.05	1 46 21.74	122	0.831	APL	2.00	$22.77^{+22.97}_{-22.54}$	32.93	230.29	263.22	43.83	43.93	44.19
XMMC J100130.33+014305.0	2299	10 01 30.33	1 43 04.97	110	1.571	PL	2.00	...	76.83	96.53	173.35	44.09	44.19	44.44
XMMC J100143.54+015606.2	2361	10 01 43.54	1 56 06.18	195	2.181	PL	$1.94^{+2.24}_{-1.68}$	...	93.06	127.11	220.17	44.52	44.66	44.90
XMMC J100240.34+020146.4	2370	10 02 40.34	2 01 46.37	132	0.638	APL	2.00	$22.16^{+22.69}_{-21.76}$	34.05	103.02	137.07	43.17	43.27	43.52
XMMC J100141.54+020051.4	2557	10 01 41.54	2 00 51.44	120	2.277	PL	2.00	...	158.62	199.31	357.93	44.80	44.90	45.15
XMMC J100142.26+020358.5	2608	10 01 42.26	2 03 58.49	131	0.125	PEXRAV+Fe	2.00	>24.18	28.99	511.11	540.01	41.07	42.32	43.87
XMMC J100136.21+015442.5	2703	10 01 36.21	1 54 42.45	151	2.281	PL	2.00	...	209.26	262.93	472.19	44.92	45.02	45.27

[a] IAU name.
[b] Internal reference number.
[c] X-ray coordinates. Units of right ascension are hours, minutes, and seconds, and units of declination are degrees, arcminutes, and arcseconds.
[d] Net pn counts in the 0.3–10 keV energy band.
[e] Spectroscopic redshift of the most likely optical counterpart (for details see Brusa et al. 2007).
[f] Best-fit model as discussed in § 4.
[g] X-ray fluxes from the spectral fit in units of 10^{-16} ergs cm^{-2} s^{-1} in the 0.5–2, 2–10, and 0.5–10 keV rest-frame energy bands, respectively.
[h] Logarithm of the X-ray luminosities corrected for absorption in the 0.5–2, 2–10, and 0.5–10 keV rest-frame energy bands, respectively.
[i] A power-law model is not a good representation of this source (see § 4.1).

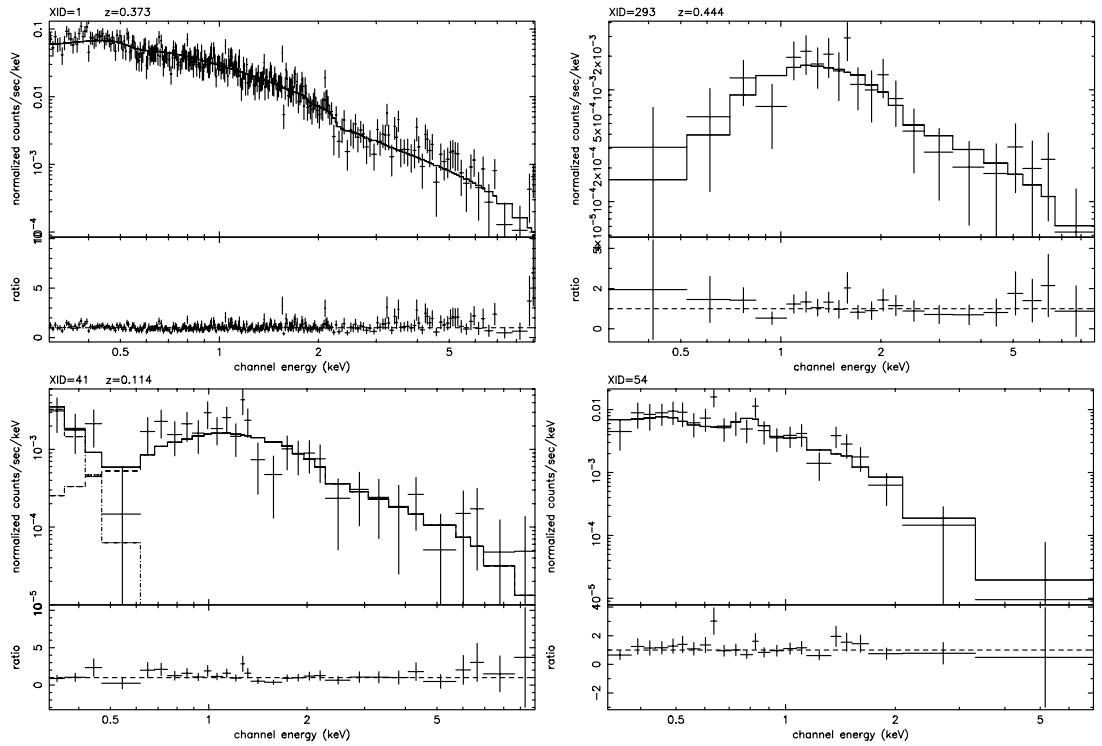

FIG. 4.— Examples of X-ray spectra with different best-fit model. *Top left*: Unabsorbed power law (PL); *top right*: absorbed power law (APL); *bottom left*: absorbed power law plus a blackbody component to model the soft excess; *bottom right*: thermal emission parameterized with a Raymond-Smith model.

2004; Gallo et al. 2006), but its origin is still uncertain. Such a soft component may be the high-energy tail of the UV bump (a blackbody model is appropriate in this case), or can be due to reprocessed emission scattered along our line of sight by a photoionized gas located just above the obscuring torus (an additional power law with the spectral index fixed to the value of the hard X-ray primary power law is a good parameterization of this scenario). We fit these four sources adding to the basic APL model an extra component represented either by a power law (po) or a blackbody (bb[22]) according to the two physical scenarios mentioned above. We report in Table 2 the parameters of the additional component in the fit of these four sources. We are not able to distinguish on a statistical basis between the two models given the similar values of χ^2. Nevertheless, we notice that all these four sources present intrinsic absorption and therefore we exclude that the soft excess of these objects is due to the high-energy tail of the UV bump (APL+bb).

[22] This is a blackbody spectrum defined by the temperature kT in keV and a normalization factor.

4.1.2. Fe Kα *Line*

Three sources show significant features ascribable to the redshifted Fe Kα emission line: xid 2028, 2043, and 2608. For these sources we add a Gaussian component (`gauss`) to the model, fixing the line energy to $6.4/(1+z)$ keV. The best-fit values of interesting parameters are reported in Table 3. We show in Figure 5 the ratio of the data versus the model (`powerlaw` for xid 2028,

TABLE 2
PARAMETERS OF THE BEST-FIT MODEL FOR SOURCES WITH SOFT EXCESS

XID	Counts[a]	Model[b]	χ^2/dof	Γ[c]	N_H[d]	kT[e]	Γ[f]	Redshift	Optical Class[g]
41.....	315	APL+po	0.94	$1.72^{+2.57}_{-1.38}$	$21.38^{+21.59}_{-21.02}$		2.0	0.114	NLAGN
		APL+bb	0.83	$1.95^{+2.37}_{-1.65}$	$21.51^{+21.55}_{-20.42}$	30^{+2}_{-3}			
106.....	141	APL+po	0.25	2.0	$22.33^{+22.66}_{-21.98}$		2.0	0.710	gal
		APL+bb	0.26	2.0	$22.28^{+23.00}_{-21.96}$	121^{+914}_{-71}			
117.....	111	APL+po	0.69	2.0	$22.76^{+23.14}_{-22.37}$		2.0	0.936	gal
		APL+bb	0.59	2.0	$22.57^{+22.86}_{-20.42}$	81^{+48}_{-18}			
274.....	112	APL+po	0.26	2.0	$22.67^{+23.00}_{-22.18}$		2.0	0.677	gal
		APL+bb	0.24	2.0	$22.55^{+23.00}_{-20.42}$	124^{+878}_{-119}			

[a] Net pn counts in the 0.3–10 keV energy range.
[b] Best-fit model: APL+po=absorbed power law plus an extra power law for the soft excess; APL+bb=absorbed power law plus a blackbody for the soft excess.
[c] Slope of the power-law model (photon index).
[d] Logarithm of the intrinsic absorption (cm^{-2}).
[e] Temperature (in eV) of the blackbody used to model the soft excess.
[f] Slope of the extra power law used to model the soft excess.
[g] Optical classification; see § 6 for details.

TABLE 3
PARAMETERS OF THE gauss ADDITIONAL COMPONENT FOR THE SOURCES WITH Fe LINE

XID	σ[a]	EW[b]	Redshift	Optical Class[c]
2028.....	616^{+364}_{-224}	2754^{+1628}_{-1002}	0.784	gal
2043.....	179^{+120}_{-115}	748^{+502}_{-481}	0.668	gal
2608.....	281^{+408}_{-175}	792^{+1151}_{-493}	0.125	gal

[a] Observed width of the line in eV.
[b] Rest-frame equivalent width of the line in eV.
[c] Optical classification; see § 6 for details.

2043 and pexrav[23] for xid 2608) in an energy range around the expected location of the Fe Kα line. Interestingly all three of these sources do not show sign of AGN activity from their optical spectra and are therefore classified as "galaxy."

4.1.3. *Thermal Emission?*

Source xid 54, if fitted with an APL model, gives a large value for the spectral slope ($\Gamma > 3$) and significant residuals in the 0.3–10 keV energy range. An alternative description of its spectrum is obtained assuming we are observing thermal emission, parameterized with a Raymond-Smith model (Raymond & Smith 1977) with a temperature $kT = 1.6^{+0.4}_{-0.2}$ keV fixing the metallicity to 0.3 solar. Source xid 54 is identified with two interacting galaxies (see Fig. 6) at redshift $z = 0.350$ with no sign of AGN activity from its optical spectrum. Its X-ray luminosity of 3×10^{42} ergs s^{-1} is larger than that expected for early-type galaxies (Matsushita 2001) and, from the optical imaging, there is a concentration of galaxies around xid 54 with the same photometric redshifts therefore supporting the idea that we are looking at the X-ray emission from a group of galaxies. Nevertheless, we cannot exclude with the current data that a fraction of the X-ray flux of source 54 could come from an absorbed nucleus (e.g., XBONGS; Comastri et al. 2002) or from discrete sources like LMXBs or HMXBs in the galaxy. A *Chandra* observation with its higher angular resolution could possibly locate discrete sources inside xid 54.

4.1.4. *XID 2608: A Compton-Thick AGN?*

An additional source that requires a more complex modeling of its spectrum is xid 2608. The fit with the APL model gives an extremely flat value for Γ ($\approx$0.3) and large residuals at both low and high energies (see Fig. 7, *left*). Hasinger et al. (2007) found that this source is located in an area populated by local Compton-thick Seyfert 2 galaxies in an X-ray color-color diagram (see Fig. 12 of Guainazzi et al. 2005). This, together with other evidences based on lines ratios from the optical spectrum, supports the hypothesis that source 2608 is a heavily absorbed AGN.

We use the 131 net counts from the pn camera for this source to study more in detail its X-ray spectrum. A pure reflection component model (pexrav) is a better description than the APL model according to an *F*-test with a confidence level of 95%. Nevertheless, this fit leaves a clear residual around the expected position of the 6.4 keV Fe Kα line. The best-fit model for xid 2608 is a pure reflection model plus a Gaussian line at 6.4 keV

[23] An exponentially cut off power-law spectrum reflected from neutral material. We refer the reader to Magdziarz & Zdziarski (1995) for a detailed description of such a model.

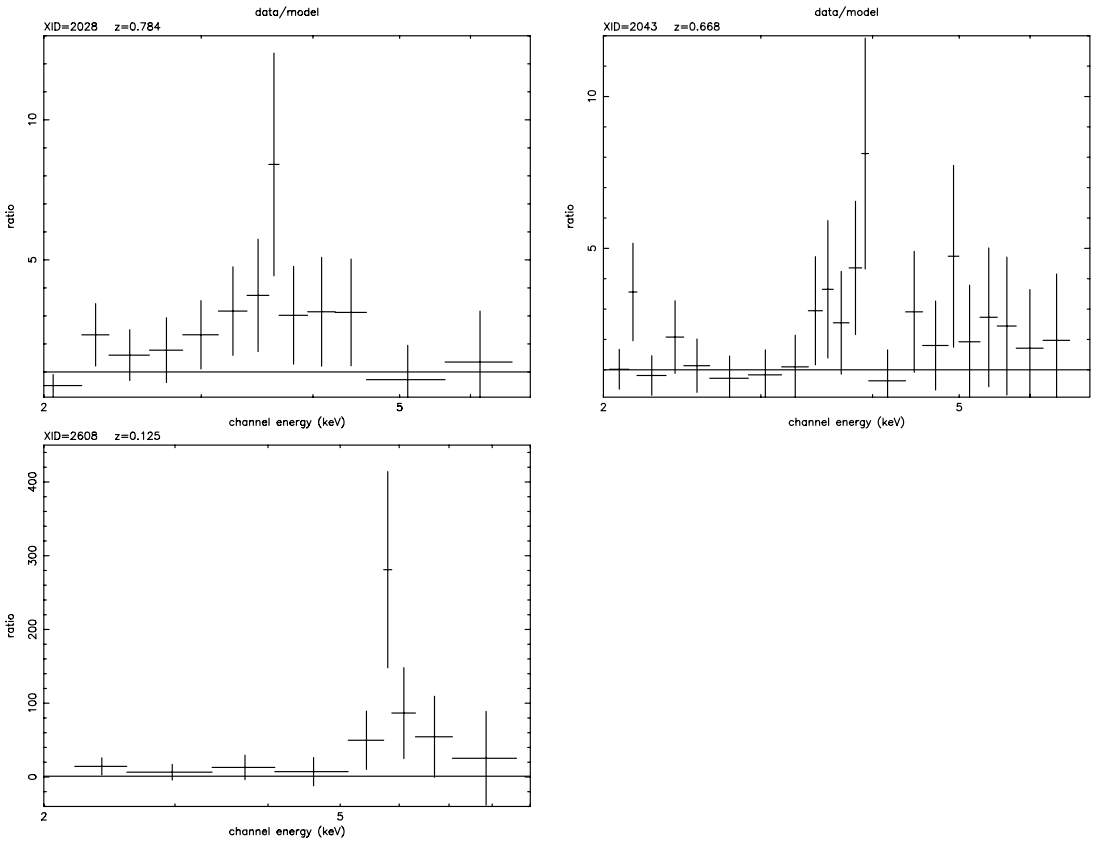

FIG. 5.—Ratio of the data vs. a powerlaw model (*top*) or a pexrav model (*bottom*) around the energy of the Fe Kα line for the three sources with significant detection of this feature.

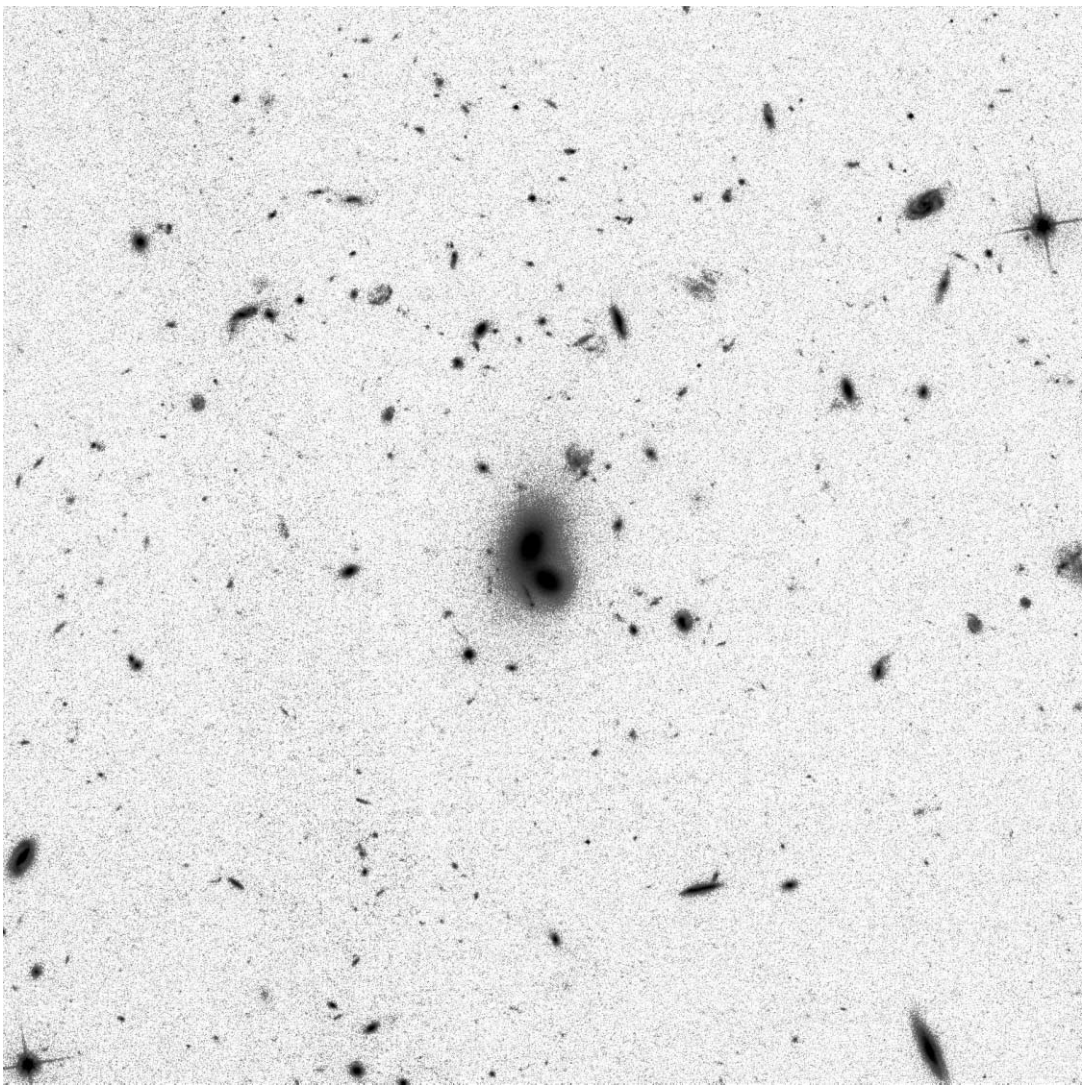

FIG. 6.—ACS image of source xid 54. The cutout is 90″ on a side.

rest frame (`pexrav+gauss`). The details for the different spectral fits are reported in Table 4. The presence of the Fe Kα fluorescent line at 6.4 keV is significant at 95% according to an *F*-test. The presence of the line is a clear sign that the source is heavily absorbed, but a useful observable to confirm its Compton-thick nature is the equivalent width (EW) of the same line. The nominal best-fit value for the EW (792^{+1151}_{-493} eV) is higher than the maximum (600 eV) observed EW in Compton-thin objects (Turner et al. 1997). This supports the idea that source 2608 is a Compton-thick AGN, although we have to mention that with the current

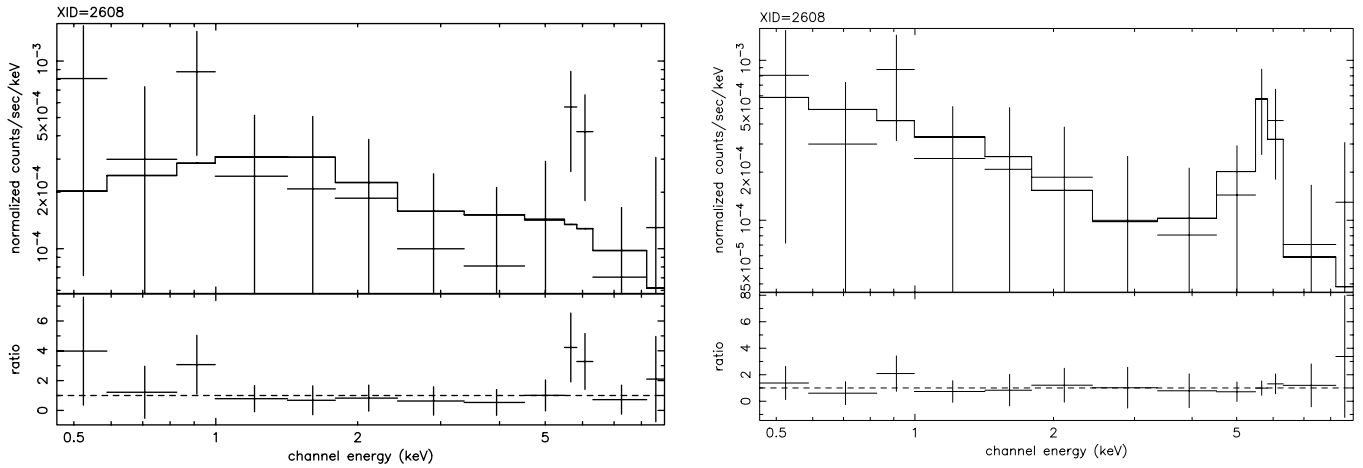

FIG. 7.—X-ray fit of source xid 2608 with the basic APL model (*left*) and a pure reflection model plus a Gaussian line (*right*).

TABLE 4
PARAMETERS OF THE BEST-FIT MODEL FOR SOURCE XID 2608

Model[a]	Γ	N_H[b]	EW[c]	χ^2	dof
APL	2.0	$0.16^{+0.75}_{-0.16}$	...	9.3	11
pexrav	2.0	...	...	4.1	9
pexrav+gauss	2.0	...	792^{+1151}_{-493}	1.7	7

[a] Best-fit model: APL = absorbed power law; pexrav = pure reflection model; pexrav+gauss = pure reflection model plus a Gaussian line.
[b] Hydrogen column density in units of 10^{22} cm^{-2}.
[c] Equivalent width of the Fe Kα line expressed in eV.

photons statistics, the error for the observed flux of the line (and consequently for the EW) is still large. We are confident that an improved result will come after the completion of the additional 600 ks *XMM-Newton* observations awarded in AO4. Another diagnostic on the Compton-thick nature of this source could be the "thickness parameter" $T = F(2-10\ \mathrm{keV})/F[\mathrm{O\ III}]$. A high-quality optical spectrum for this source is available in the Sloan Digital Sky Survey archive, and we obtain a value for $F[\mathrm{O\ III}]$ from the analysis of Kauffmann et al. (2003). The [O III] flux has been corrected for the extinction toward the narrow-line region as deduced from the Balmer decrement. We obtain $T = 3.8$, which is in a "gray area" where both Compton-thick and less absorbed AGNs are located (see, e.g., Fig. 1 of Bassani et al. 1999).

In Figure 13 below, we assume as a lower limit for the column density of xid 2608 the value 1.5×10^{24} cm^{-2}, where the Compton optical depth is equal to unity and the directly transmitted nuclear emission is strongly suppressed in the 0.3–10 keV band. For the luminosity of this object, if we assume that only 3% of the flux has been reflected, we obtain a value of $\sim 7.4 \times 10^{43}$ ergs s^{-1}, while for reflected fractions between 10% and 1%, the luminosity would be in the range $(0.2-2.2) \times 10^{44}$ ergs s^{-1}.

4.2. *Spectral Properties of the Sample*

As mentioned in § 4, we leave both Γ and N_H free to vary when fitting the sources in sample 1. The results of this analysis are summarized in Figure 8. The average value of Γ does not change as a function of N_H, as already noticed in deep surveys (i.e., Mainieri et al. 2002). We obtain, using the weighted mean, $\langle\Gamma\rangle = 2.06 \pm 0.08$, and the observed dispersion of the distribution of the best-fit values is $\sigma \approx 0.25$. As the typical error in a single measurement of Γ is $\Delta\Gamma = 0.09$, assuming that both statistical errors and the intrinsic dispersion are distributed as a Gaussian, the intrinsic scatter in Γ is $\sigma_{\mathrm{int}} \sim 0.24$. For comparison with X-ray spectral studies in a similar X-ray flux range of our sample, Mateos et al. (2005a) from a large sample of serendipitous sources detected with *XMM-Newton* in a ~ 3.5 deg^2 area, obtained $\langle\Gamma\rangle = 1.96 \pm 0.01$; Perola et al. (2004) in the spectroscopic analysis of the HELLAS2XMM 1df found $\langle\Gamma\rangle = 1.90 \pm 0.22$; Page et al. (2006) from the spectral fit of AGNs in the 13^H *XMM-Newton*/*Chandra* deep field found $\langle\Gamma\rangle = 2.0 \pm 0.1$ with an intrinsic dispersion $\sigma \approx 0.36$. All these measurements are consistent with each other within the uncertainties. If we adopt the optical classification described in § 2, the mean value for the spectral slope for BL AGNs (58 sources) is $\langle\Gamma\rangle = 2.09$ with a dispersion of $\sigma \approx 0.26$, while for NOT BL AGNs (24 sources) we obtain $\langle\Gamma\rangle = 1.93$ and $\sigma \approx 0.29$. Furthermore, we confirm that the average value of the photon index does not vary with redshift in the range $z = [0.0, 3.0]$ covered by our sample, thus confirming previous findings (e.g., see Fig. 9 of Piconcelli et al. (2003) for a compilation from the literature.

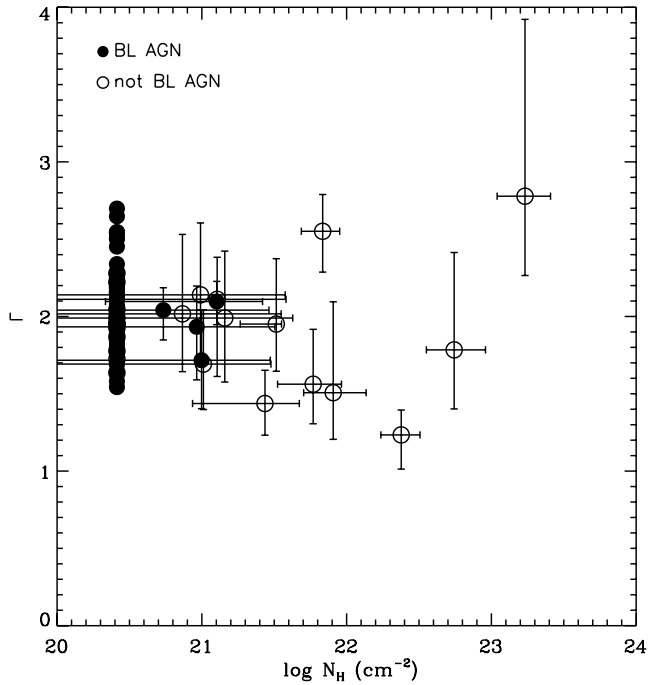

FIG. 8.—Γ vs. N_H for the X-ray sources with more than 180 net counts in 0.3–10 keV (bright sample) and spectroscopically identified. Filled circles are BL AGNs, while open circles are NOT BL AGNs. Error bars correspond to 1 σ. To simplify the figure, we did not report the error bars on Γ for unabsorbed sources and plotted them to $N_H = N_H^{\mathrm{Gal}} \approx 2.7 \times 10^{20}$ cm^{-2}. [*See the electronic edition of the Supplement for a color version of this figure*.]

The other physical quantity that we measure from the spectral fitting is the column density N_H. In this case, we consider all our 135 sources since N_H has been left free to vary in both sample 1 and sample 2. According to an *F*-test, 32 X-ray sources do require intrinsic absorption in excess to the Galactic one, at a confidence level larger than 90%. Therefore a fraction as large as 24% of our sample is made of X-ray-absorbed AGNs. Figure 9 shows the distribution of N_H values for these sources. We note that the observed N_H distribution refers only to the sources inside the region in the N_H-L_X-z space delimited by the count-rate detection threshold of our survey. This introduces a bias against absorbed sources, and therefore the fraction of absorbed sources detected in our study has to be considered a lower limit. According to the most recent population synthesis model of the XRB (Gilli et al. 2007), in the band used to select our sample, the expected fraction of obscured source with column density $N_H > 10^{21}$ cm^{-2} is 20% that is consistent with what we found. In Figure 9 we divide BL AGNs from NOT BL AGNs. The visual impression that NOT BL AGNs have larger column densities than BL AGNs is confirmed by a Kolmogorov-Smirnov test that gives a probability larger than 99.9% that the two distributions are different. No object with $N_H > 10^{22}$ cm^{-2} shows broad lines in its optical spectrum. Nevertheless, 9% (8/86) of the BL AGNs in our sample do show some intrinsic absorption in their X-ray spectra (see also Mittaz et al. 1999; Fiore et al. 2001; Page et al. 2001; Schartel et al. 1997; Tozzi et al. 2001; Mainieri et al. 2002; Brusa et al. 2003; Perola et al. 2004; Mateos et al. 2005b). In Figure 10 we show the distributions of the $R-K$ (Vega) colors for the sources with PL as best-fit model (*open histogram*) and for the ones that instead require an absorbed power law (*hatched histogram*). The two distributions are significantly different according to a Kolmogorov-Smirnov test with a probability of 99.99%. The X-ray sources that require an absorption component in their spectral fit are on average

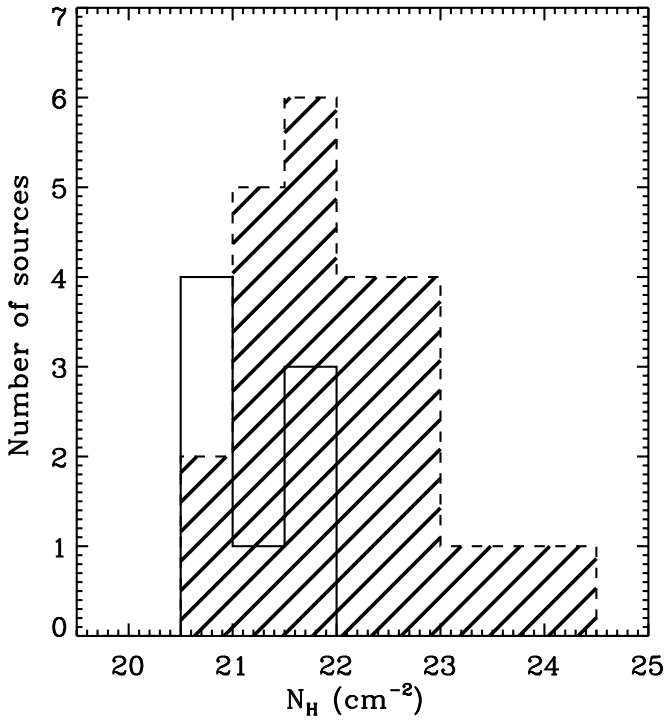

FIG. 9.—Intrinsic column density ($N_{\rm H}$) distribution for BL AGNs (*open histogram*) and NOT BL AGNs (*hatched histogram*) with intrinsic absorption in excess of the Galactic column density. [*See the electronic edition of the Supplement for a color version of this figure*.]

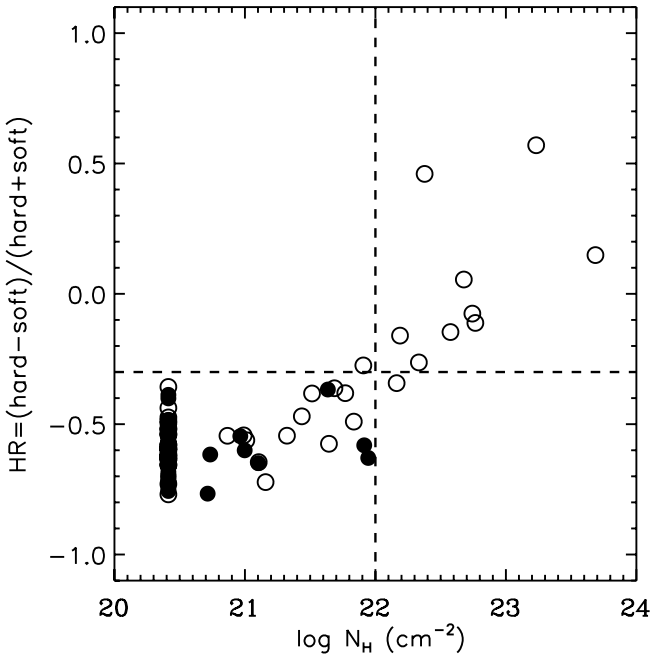

FIG. 11.—HR defined using the 0.5–2 (soft) and 2–10 (hard) bands vs. the column density derived from the spectral fitting analysis. Only sources with errors on the HR smaller than 0.3 have been plotted. Filled circles are BL AGNs, while open circles are NOT BL AGNs. The horizontal dashed line corresponds to HR $= -0.3$ used to separate absorbed and unabsorbed sources, while the vertical dashed line indicates a column density equal to 10^{22} cm^{-2}. [*See the electronic edition of the Supplement for a color version of this figure*.]

redder, suggesting a correlation between X-ray absorption and optical to near-IR colors. On the contrary, sources that do not show absorption in their X-ray spectra have bluer color typical of optically selected, unobscured quasars. These results confirm those obtained from an analysis based on HR values made by Brusa et al. (2007; see their Fig. 10). Nevertheless the interpretation of this correlation between X-ray absorption and optical to near-IR colors is not straightforward since we are sampling different scales in the two measurements (i.e., nucleus with the X-ray data and nucleus+host galaxy with the $R-K$ colors).

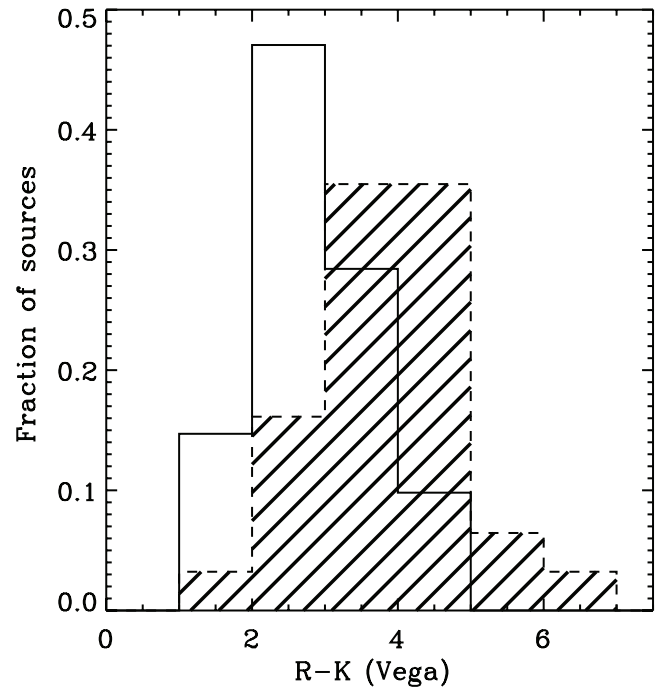

FIG. 10.—$R-K$ colors (Vega) distribution for sources with PL as best-fit model (*open histogram*) and for sources with APL as a best-fit model (*hatched histogram*). [*See the electronic edition of the Supplement for a color version of this figure*.]

When the number of counts in a source is inadequate to perform a spectral fit, a widely used tool to study the general spectral properties of an X-ray source is the hardness ratio HR $= (H - S)/(H + S)$, where H are the counts in the 2–4.5 keV band and S those in the 0.5–2 keV energy band. In Figure 11 we show the hardness ratio values versus the amount of intrinsic absorption derived from our spectral analysis (both sample 1 and sample 2). A clear correlation between the two quantities is present: 90%[24] of the sources with $N_{\rm H} > 10^{22}$ cm^{-2} have HR > -0.3 and 99% of the sources with $N_{\rm H} < 10^{22}$ cm^{-2} have HR < -0.3. Therefore, although one has to remember that the HR is a strong function of redshift (e.g., Fig. 8 in Szokoly et al. 2004), it is still possible to use HR for statistical studies.

Another diagnostic that can yield important information on the nature of X-ray sources is the X-ray-to-optical flux ratio (e.g., Maccacaro et al. 1988; Stocke et al. 1991). The majority of the AGNs have X-ray-to-optical flux ratios (X/O) of $0.1 <$ X/O < 10 (e.g., Akiyama et al. 2000; Lehmann et al. 2001), but *Chandra* and *XMM-Newton* surveys have shown that there is a non-negligible population of AGNs with high X/O (>10) and that a large fraction of them are obscured, and possibly high-redshift, type 2 QSOs (e.g., Fabian et al. 2000; Mainieri et al. 2002, 2005; Fiore et al. 2003; Mignoli et al. 2004). For comparison with the literature, we define X/O as the ratio between the X-ray flux in the 2–10 keV band and the flux in the optical R

[24] We note that the only source with $N_{\rm H} > 10^{22}$ cm^{-2} and HR < -0.3 shows a soft excess in its X-ray spectrum.

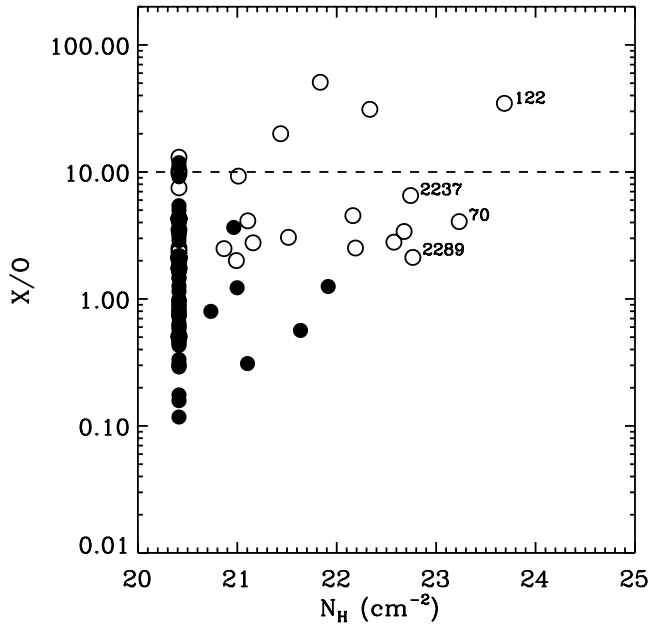

FIG. 12.—X/O [$f(2–10\ \mathrm{keV})/F(R)$] vs. N_H values. The filled circles are BL AGNs, the open circles NOT BL AGNs. We label the four type 2 QSOs candidates. The horizontal dashed line indicates the value X/O = 10. [*See the electronic edition of the Supplement for a color version of this figure*.]

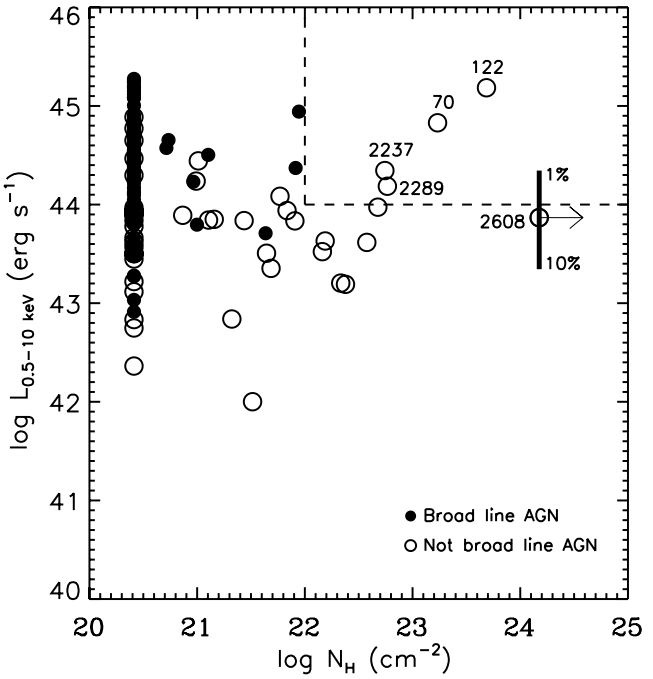

FIG. 13.—Intrinsic, de-absorbed X-ray luminosity in the 0.5–10 keV band vs. N_H. The filled symbols are BL AGNs, while the open symbols are NOT BL AGNs. For source xid 2608 we assume a lower limit on N_H of 1.5×10^{24} cm^{-2} and for the luminosity we estimate a value of $\sim 7.4 \times 10^{43}$ ergs s^{-1} assuming that a fraction of 3% is reflected (the error bar shows the luminosity range covered assuming that the reflected fraction is between 1% and 10%). See § 4.1.4 for details. The dashed lines define the type 2 QSO region. [*See the electronic edition of the Supplement for a color version of this figure*.]

band. In Figure 12 we plot the X/O values for the sources in our sample versus the N_H. Out of the seven sources that have X/O > 10, four show absorption in their X-ray spectra (APL) and one is a type 2 QSO. We notice that the other three type 2 QSO candidates in our sample (see § 5) have X/O values inside the range $0.1 < \mathrm{X/O} < 10$, where most of the optical or soft X-ray-selected AGNs are located. Since we limit our analysis to the brighter X-ray sources and the spectroscopic follow-up is not complete, we postpone any further analysis on the nature of X/O > 10 sources to a future paper.

5. TYPE 2 QSO CANDIDATES

Using the spectral parameters from the best-fit model, we correct the X-ray luminosity of each source for the intrinsic and Galactic absorption. These corrected luminosities are plotted in Figure 13 versus the N_H for all the sources in our sample. Four objects are characterized by a high X-ray luminosity ($L_X[0.5–10\ \mathrm{keV}] > 10^{44}$ ergs s^{-1}) and substantial absorption ($N_H > 10^{22}$ cm^{-2}) and we can therefore classify them as type 2 QSOs. Radio-loud type 2 QSOs are known since long times thanks to radio surveys (see McCarthy 1993 for a comprehensive review), while radio-quiet type 2 QSOs have been observed only recently in *Chandra* and *XMM-Newton* X-ray surveys (Dawson et al. 2001; Norman et al. 2002; Mainieri et al. 2002; Stern et al. 2002; Della Ceca et al. 2003; Fiore et al. 2003; Tozzi et al. 2006) and optical surveys (SDSS; Zakamska et al. 2005). Two of our type 2 QSOs candidates, xid = 70 and 2289, are clearly detected in the radio at 20 cm using the Very Large Array (VLA) with an integrated flux of 540 ± 24 and 52 ± 11 μJy, respectively (Schinnerer et al. 2007). The radio power of these two sources is therefore $P_{1.4\ \mathrm{GHz}} = 9.8 \times 10^{23}$ and 1.5×10^{23} W Hz^{-1}. Historically such radio power has been used to divide radio-loud and radio-quiet AGNs, but such a dividing line appears to be redshift dependent: $\approx 5 \times 10^{23}$ W Hz^{-1} for the Palomar Green sample (mainly below $z < 0.3$) up to 5×10^{25} W Hz^{-1} for the Large Bright Quasar Survey sample ($\langle z \rangle \sim 1.2$). Since our two sources are at $z \sim 0.7–0.8$, we suggest to classify them as radio-quiet AGNs. The other two objects (xid = 122, 2237) are not detected in the radio and we can fix a 4.5 σ upper limit to their radio flux of 50 and 54 μJy (Schinnerer et al. 2007). The optical spectra of these four sources show high-excitation emission lines and their redshifts are 0.688, 0.831, 0.941, and 2.418, respectively, for xid 70, 2289, 2237, and 122. Using the multiband photometry available from the COSMOS survey (Capak et al. 2007), we have derived the spectral energy distribution (SED) for the four type 2 QSOs and compared them with the spectrum of NGC 6240 and a Seyfert 2 composite spectrum derived from a sample of local galaxies by Schmitt et al. (1997) and Moran et al. (2001). While the SED of NGC 6240 does not reproduce well the observed photometry of our type 2 QSOs, an excellent description of the same is given by the composite Seyfert 2 SED (see Fig. 14, *right*). Furthermore, the $R-K$ colors of these four objects are red ($R - K = 4.58, 3.91, 4.97$, and 4.76, respectively), although they cannot be classified as extremely red objects (EROs; $R - K > 5$).

6. COMPARISON BETWEEN X-RAY AND OPTICAL CLASSIFICATIONS

A classification based on the properties of the optical spectra of the 135 sources in our sample divides them into "broad-line AGNs" (BL AGNs; 86 objects) if emission lines broader than 2000 km s^{-1} are present, "narrow-line AGNs" (NL AGNs; 32 objects) if the optical spectrum shows high-excitation emission lines, and "galaxy" (gal; 17 objects) if there is no sign of AGN activity from the optical spectrum. As shown by deep *Chandra* and *XMM-Newton* surveys (e.g., Szokoly et al. 2004), a pure optical classification of AGNs is biased against absorbed sources that appear as normal galaxies at those wavelengths. As previously done by Szokoly et al. (2004) and Tozzi et al. (2006), we introduce an X-ray based classification: we define "*X-ray-absorbed*" AGN sources that are best fitted by an APL model compared to the PL one and

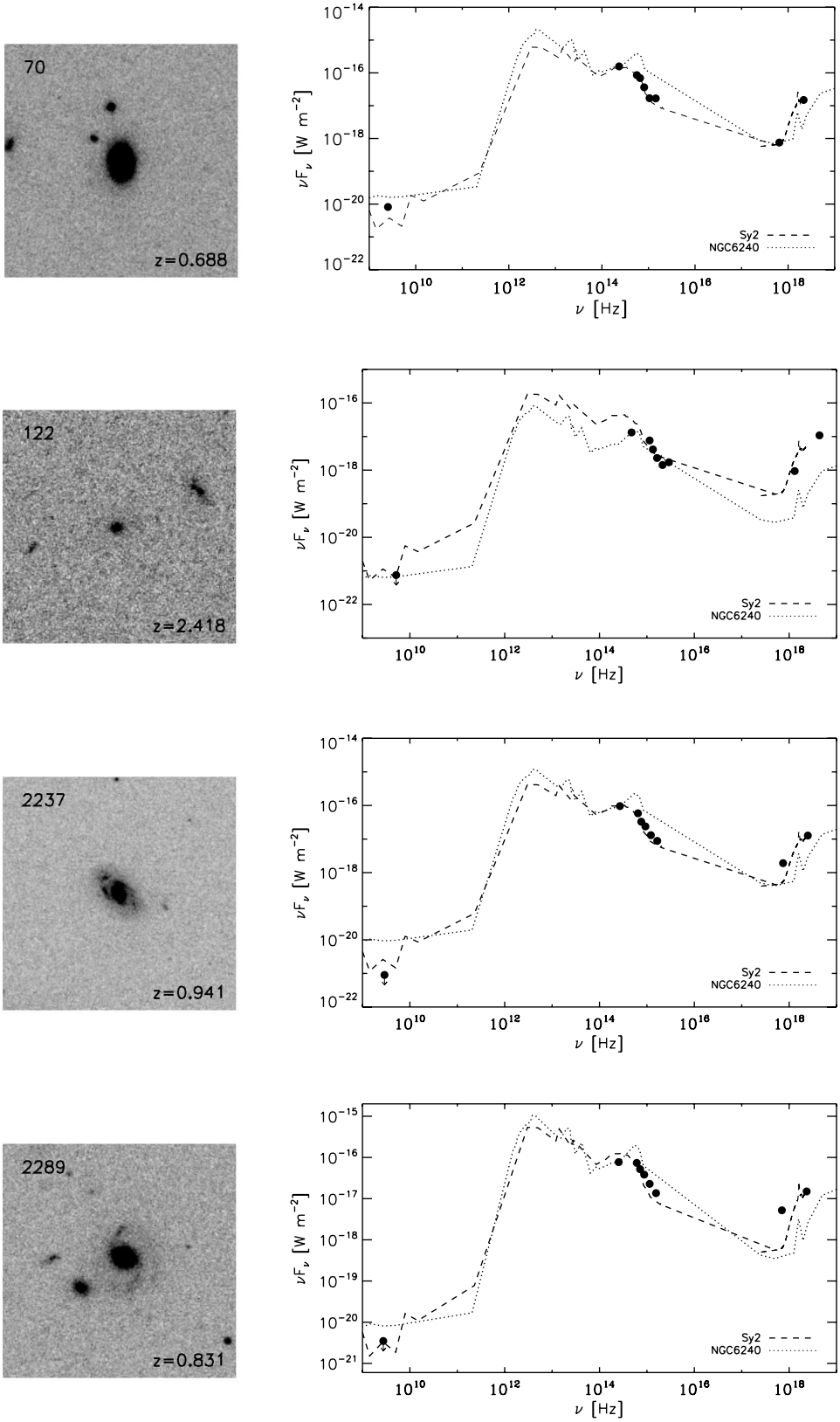

FIG. 14.—*Left*: *i*-band (F775W) ACS cutouts for the four type 2 QSO candidates. Each cutout is 10″ across. *Right*: the spectral energy distribution of the type 2 QSO candidates (*filled circles*) compared to the SED of a composite Seyfert 2 spectrum (*dashed line*) and NGC6240 (*dotted line*). [*See the electronic edition of the Supplement for a color version of this figure*.]

TABLE 5
Comparison Between Optical and X-Ray Classifications

X-Ray Classification	Broad-Line AGNs	Narrow-Line AGNs	Galaxy
X-Ray-Unabsorbed AGNs	78	19	5
X-Ray-Absorbed AGNs	8	13	11
X-Ray Galaxy	0	0	0

have $L_X > 10^{42}$ ergs s^{-1}, X-ray-unabsorbed AGN sources best fitted with a PL model and $L_X > 10^{42}$ ergs s^{-1}, and finally "X-ray galaxies" sources with $L_X < 10^{42}$ ergs s^{-1}. Table 5 shows the comparison of the optical and X-ray classifications for our 135 sources. Ninety-one of these sources ($\sim$67%) have a similar classification from the optical and X-ray data. The best agreement between the two classifications is for broad-line AGN (optical) and X-ray-unabsorbed AGN (X-ray) for which the fractions of similar classifications are of the order of 91% (78/86 broad-line AGNs) and 76% (78/102 X-ray-unabsorbed AGNs), respectively. The $\sim$9% of BL AGNs that show X-ray absorption in their X-ray spectra have values of the column density N_H below 10^{22} cm^{-2} (see open histogram in Fig. 9). The main difference is instead for objects classified as galaxies on the basis of the optical spectra. Most of these objects (16/17) are classified as AGN (11 absorbed and 5 unabsorbed) on the basis of the X-ray luminosity. This confirms that the X-ray classification is more successful than the optical one in revealing the presence of black hole activity. The situation is intermediate for narrow-line and X-ray-absorbed AGNs: only $\sim$41% of the optically classified narrow-line AGNs do show detectable X-ray absorption. We note that of the remaining narrow-line AGNs, $\sim$80% have $z > 0.4$ and therefore the Hα line is outside the observed wavelength range, while for nine of them the Mg [II] line is inside the observed range (i.e., $0.92 < z < 2.29$) but the S/N of the spectra could not be sufficient to detect a weak broad line. It is therefore possible that at least part of the disagreement between the optical and the X-ray classifications for these objects is due to less than optimal optical spectra, in terms of either spectral coverage or S/N.

7. CONCLUSIONS

We have presented the detailed spectral analysis of 135 X-ray sources from the *XMM-Newton* wide-field survey in the COSMOS field. All the sources in our sample have more than 100 net counts in the 0.3–10 keV energy band and have been spectroscopically identified. For each source we have performed an accurate spectral fit in order to measure the continuum shape, the amount of absorbing matter, and the strength of other spectral features. Our main results are summarized as follows:

1. We find that, to the X-ray flux limit we are sampling ($F_X[0.5–10] = 1.4 \times 10^{-15}$ ergs cm^{-2} s^{-1}), $\sim$76% of the spectra are well reproduced with a single power-law model, $\sim$20% require an absorbed power-law model, and the remaining $\sim$4% need more complex models.

2. The average value of the spectral slope of the intrinsic spectrum for the 82 sources with more than 180 net counts (sample 1) is $\langle\Gamma\rangle = 2.06 \pm 0.08$ with an intrinsic dispersion of $\sigma_{int} = 0.24$.

3. We find no correlation between the spectral slope Γ and the amount of intrinsic absorption N_H, confirming that the hardening of the X-ray spectra going to fainter X-ray fluxes is due to the increased fraction of absorbed X-ray sources.

4. None of the X-ray sources with a column density $N_H > 10^{22}$ cm^{-2} shows broad lines in their optical spectra, although a fraction (9%) of broad-line AGNs shows intrinsic absorption in excess to the Galactic value.

5. We detect (at more than 90% confidence level) the Fe Kα line in three objects. One of them is well described by a pure reflection model plus a Gaussian line at 6.4 keV rest frame. This, the large equivalent width of the Fe line (although with large uncertainties), and diagnostics based on lines ratios from the optical spectrum support the hypothesis that this particular source is a Compton-thick AGN.

6. We find four radio-quiet type 2 QSOs. Their spectral energy distribution is well reproduced with a Seyfert 2 composite spectrum.

7. We confirm that in order to have a less biased sample of AGNs it is crucial to complement the optical spectral properties with the X-ray informations (L_X and N_H), since many apparently normal galaxies in the optical band are instead absorbed AGNs.

This is the first work on the X-ray spectral properties of the AGNs in the COSMOS survey. We remark that once the *XMM-Newton* observations is completed and the planned spectroscopic follow-up finished, we will be able to analyze the X-ray spectral properties of the AGNs on a much larger sample and compare them with the properties of the AGNs/host galaxies at almost all the wavelengths.

This work is based on observations obtained with *XMM-Newton*, an ESA science mission with instruments and contributions directly funded by ESA Member States and the US (NASA). In Germany, the *XMM-Newton* project is supported by the Bundesministerium für Wirtschaft und Technologie/Deutsches Zentrum für Luft- und Raumfahrt (BMWI/DLR, FKZ 50 OX 0001), the Max-Planck Society and the Heidenhain-Stiftung. Part of this work was supported by the Deutsches Zentrum für Luft- und Raumfahrt, DLR project numbers 50 OR 0207 and 50 OR 0405. In Italy, the COSMOS *XMM-Newton* project is supported by INAF and MIUR under grants PRIN/270/2003 and Cofin-03-02-23. Based on observations with the NASA/ESA *Hubble Space Telescope*, obtained at the Space Telescope Science Institute, which is operated by AURA, Inc., under NASA contract NAS5-26555. The *HST* COSMOS Treasury program was supported through NASA grant HST-GO-09822. Also based on data collected at the Subaru Telescope, which is operated by the National Astronomical Observatory of Japan; the European Southern Observatory under Large Program 175.A-0839, Chile; and the National Radio Astronomy Observatory, which is a facility of the National Science Foundation operated under cooperative agreement by Associated Universities, Inc. We are grateful to Paolo Tozzi, Kazushi Iwasawa, and Paolo Padovani for inspiring discussions. We gratefully acknowledge the entire COSMOS collaboration consisting of more than 70 scientists. More information on the COSMOS survey is available at http://www.astro.caltech.edu/~cosmos. It is a pleasure the acknowledge the excellent services provided by the NASA IPAC/IRSA staff (Anastasia Laity, Anastasia Alexov, Bruce Berriman, and John Good) in providing online archive and server capabilities for the COSMOS data sets.

REFERENCES

Akiyama, M., et al. 2000, ApJ, 532, 700
Alexander, D. M., et al. 2003, AJ, 126, 539
Arnaud, K. A., et al. 1985, MNRAS, 217, 105
Bassani, L., Dadina, M., Maiolino, R., Salvati, M., Risaliti, G., della Ceca, R., Matt, G., & Zamorani, G. 1999, ApJS, 121, 473
Brandt, W. N., et al. 2001, AJ, 122, 2810
Brusa, M., et al. 2003, A&A, 409, 65
———. 2007, ApJS, 172, 353
Capak, P., et al. 2007, ApJS, 172, 99
Cappelluti, N., et al. 2007, ApJS, 172, 341
Cash, W. 1979, ApJ, 228, 939
Comastri, A., Setti, G., Zamorani, G., & Hasinger, G. 1995, A&A, 296, 1
Comastri, A., et al. 2002, ApJ, 571, 771
Cowie, L. L., Garmire, G. P., Bautz, M. W., Barger, A. J., Brandt, W. N., & Hornschemeier, A. E. 2002, ApJ, 566, L5
Dawson, S., Stern, D., Bunker, A. J., Spinrad, H., & Dey, A. 2001, AJ, 122, 598
Della Ceca, R., et al. 2003, A&A, 406, 555
Dickey, J. M., & Lockman, F. J. 1990, ARA&A, 28, 215
Fabian, A. C., et al. 2000, MNRAS, 315, L8
Fiore, F., et al. 2001, MNRAS, 327, 771
———. 2003, A&A, 409, 79
Gallo, L. C., Lehmann, I., Pietsch, W., Boller, T., Brinkmann, W., Friedrich, P., & Grupe, D. 2006, MNRAS, 365, 688
Gilli, R., Comastri, A., & Hasinger, G. 2007, A&A, 463, 79
Gilli, R., Salvati, M., & Hasinger, G. 2001, A&A, 366, 407
Guainazzi, M., Matt, G., & Perola, G. C. 2005, A&A, 444, 119
Hasinger, G., Burg, R., Giacconi, R., Schmidt, M., Trumper, J., & Zamorani, G. 1998, A&A, 329, 482
Hasinger, G., et al. 2001, A&A, 365, L45
———. 2007, ApJS, 172, 29
Kauffmann, G., et al. 2003, MNRAS, 346, 1055
Lehmann, I., et al. 2001, A&A, 371, 833
Lilly, S., et al. 2007, ApJS, 172, 70
Loaring, N. S., et al. 2005, MNRAS, 362, 1371
Maccacaro, T., Gioia, I. M., Wolter, A., Zamorani, G., & Stocke, J. T. 1988, ApJ, 326, 680
Magdziarz, P., & Zdziarski. A. A. 1995, MNRAS, 273, 837
Mainieri, V., Bergeron, J., Hasinger, G., Lehmann, I., Rosati, P., Schmidt, M., Szokoly, G., & Della Ceca, R. 2002, A&A, 393, 425
Mainieri, V., et al. 2005, A&A, 437, 805
Martinez-Sansigre, A., Rawlings, S., Lacy, M., Fadda, D., Marleau, F. R., Simpson, C., Willott, C. J., & Jarvis, M. J. 2005, Nature, 436, 666
Mateos, S., Barcons, X., Carrera, F. J., Ceballos, M. T., Hasinger, G., Lehmann, I., Fabian, A. C., & Streblyanska, A. 2005b, A&A, 444, 79
Mateos, S., et al. 2005a, A&A, 433, 855
Matsushita, K. 2001, ApJ, 547, 693
McCarthy, P. J. 1993, ARA&A, 31, 639
Mignoli, M., et al. 2004, A&A, 418, 827
Mittaz, J. P. D., et al. 1999, MNRAS, 308, 233
Moran, E. C., Kay, L. E., Davis, M., Filippenko, A. V., & Barth, A. J. 2001, ApJ, 556, L75
Morrison, R., & McCammon, D. 1983, ApJ, 270, 119
Norman, C., et al. 2002, ApJ, 571, 218
Page, M. J., Mittaz, J. P. D., & Carrera, F. J. 2001, MNRAS, 325, 575
Page, M. J., et al. 2006, MNRAS, 369, 156
Perola, G. C., et al. 2004, A&A, 421, 491
Piconcelli, E., Cappi, M., Bassani, L., Di Cocco, G., & Dadina, M. 2003, A&A, 412, 689
Porquet, D., Reeves, J. N., O'Brien, P., & Brinkmann, W. 2004, A&A, 422, 85
Pounds, K., & Reeves, J. 2002, in New Visions of the X-ray Universe in the *XMM-Newton* and *Chandra* Era (Noordwijk:ESA), in press (astro-ph/0201436)
Raymond, J. C., & Smith, B. W. 1977, ApJS, 35, 419
Rosati, P., et al. 2002, ApJ, 566, 667
Schartel, N., Schmidt, M., Fink, H. H., Hasinger, G., & Truemper, J. 1997, A&A, 320, 696
Schinnerer, E., et al. 2007, ApJS, 172, 46
Schmitt, H. R., Kinney, A. L., Calzetti, D., & Storchi Bergmann, T. 1997, AJ, 114, 592
Scoville, N. Z., et al. 2007, ApJS, 172, 1
Setti, G., & Woltjer, L. 1989, A&A, 224, L21
Stern, D., et al. 2002, ApJ, 568, 71
Stocke, J. T., Morris, S. L., Gioia, I. M., Maccacaro, T., Schild, R., Wolter, A., Fleming, T. A., & Henry, J. P. 1991, ApJS, 76, 813
Strüder, L., et al. 2001, A&A, 365, L18
Szokoly, G. P., et al. 2004, ApJS, 155, 271
Tozzi, P., et al. 2001, ApJ, 562, 42
———. 2006, A&A, 451, 457
Trump, J., et al. 2007, ApJS, 172, 383
Turner, T. J., George, I. M., Nandra, K., & Mushotzky, R. F. 1997, ApJS, 113, 23
Turner, T. J., & Pounds, K. A. 1989, MNRAS, 240, 833
Worsley, M. A., et al. 2005, MNRAS, 357, 1281
Zakamska, N. L., et al. 2005, AJ, 129, 1212